J. Fluid Mech. (2017), *vol.* 823, *pp.* 391–432.
doi:10.1017/jfm.2017.294

Submesoscale surface fronts and filaments: secondary circulation, buoyancy flux, and frontogenesis

James C. McWilliams†

Department of Atmospheric and Oceanic Sciences, University of California, Los Angeles, CA 90095-1565, USA

(Received 14 July 2016; revised 9 January 2017; accepted 1 May 2017; first published online 20 June 2017)

Problems are posed and solved for upper-ocean submesoscale density fronts and filaments in the presence of surface wind stress and the associated boundary-layer turbulent mixing, their associated geostrophic and secondary circulations and their instantaneous buoyancy fluxes and frontogenetic evolutionary tendencies in both velocity and buoyancy gradients. The analysis is diagnostic rather than prognostic, and it is based on a momentum-balanced approximation that assumes the ageostrophic acceleration is negligible, although the Rossby number is finite and ageostrophic advection is included, justified by the quasi-steady, coherent-structure flow configurations of fronts and filaments. Across a wide range of wind and buoyancy-gradient parameters, the ageostrophic secondary circulation for a front is a single overturning cell with downwelling on the dense side, hence with a positive (restratifying) vertical buoyancy flux. For a dense filament the circulation is a double cell with central downwelling and again positive vertical buoyancy flux. The primary explanation for these secondary-circulation cells is a 'turbulent thermal wind' linear momentum balance. These circulation patterns, and their associated frontogenetic tendencies in both the velocity and buoyancy gradients, are qualitatively similar to those due to the 'classical' mechanism of strain-induced frontogenesis. For linear solutions, the secondary circulation and frontogenesis are essentially independent of wind direction, but in nonlinear solutions ageostrophic advection provides a strong intensification of the peak vertical velocity, while generally preserving the ageostrophic circulation pattern, when the Rossby number is order one and the wind orientation relative to the frontal axis is favourable. At large Rossby number the solution procedure fails to converge, with an implication of a failure of existence of wholly balanced circulations.

Key words: ocean processes, rotating flows, stratified flows

1. Introduction

In observations and numerical simulations, the strongest submesoscale currents in the upper ocean are often horizontal jets, fronts, filaments and vortices (McWilliams 2016). These currents are approximately in geostrophic, hydrostatic balance with the

† Email address for correspondence: jcm@atmos.ucla.edu

sea level, pressure and buoyancy fields. All of these flow configurations are 'coherent structures' that are in dynamically preferred states – i.e. attractors with respect to the nonlinear advective dynamics – with a relatively slow evolution rate t_{cs}^{-1} compared to a canonical turbulent decorrelation eddy-turnover rate for a more disordered flow configuration with comparable scales, i.e. $t_{eddy}^{-1} = V_g/\ell$, where ℓ is the cross-flow horizontal length scale and V_g is the geostrophic velocity. For example, in a vortex ℓ is the radial scale and V_g is the azimuthal velocity, and in a front or filament ℓ is the cross-axis scale and V_g is the along-axis velocity. At the submesoscale, the Rossby number ($Ro = V_g/f\ell$, where f is the local Coriolis frequency) is usually not small, but neither is it so large as to make rotational effects unimportant.

Associated with the geostrophic currents are surface boundary-layer turbulence and other ageostrophic secondary circulations. Often the horizontal buoyancy and velocity gradients sharpen in frontogenesis. Here the analysis perspective is that these nearly geostrophic currents and their evolution are governed by a complete circulation dynamics (e.g. in a general circulation model) that is simply accepted as having acted to generate the coherent structures, but it is useful to be able to diagnose and interpret the associated vertical velocity w (the secondary circulation in the plane perpendicular to the primary geostrophic flow), the advective buoyancy flux and the frontogenetic tendency through simplified diagnostic equations. This instantaneous diagnostic approach is abbreviated as SCFT (secondary circulation and frontogenetic tendency).

As the SCFT theoretical framework in this paper, a momentum-balance approximation is made based on the neglect of ageostrophic acceleration. The phenomenological targets here are submesoscale buoyancy fronts and filaments that lie substantially within the surface boundary layer. A further approximation is made of along-front symmetry (e.g. $b(x, z)$, where $b = -g\rho/\rho_0$ is the buoyancy, g is gravity, ρ is density, x is the cross-axis coordinate and z is the vertical coordinate). These two approximations preclude frontal instabilities and unbalanced dynamics (e.g. gravity waves and forward energy cascade) that can become important in more complete solutions.

The starting dynamical framework is the so-called turbulent thermal wind (TTW) balance, which is a quasi-steady horizontal momentum balance that combines Coriolis, pressure gradient and vertical momentum mixing forces; alternatively expressed, it is a synthesis of geostrophic, hydrostatic and Ekman-layer dynamics. The basic idea of a secondary circulation associated with mixing in the presence of geostrophic circulation has numerous precursors to the TTW model as formulated here (e.g. Garrett & Loder 1981; Flierl & Mied 1985; Thompson 2000; Mahadevan & Tandon 2006; Nagai, Tandon & Rudnick 2006; Cronin & Kessler 2009; Ponte *et al.* 2013; Gula, Molemaker & McWilliams 2014; McWilliams *et al.* 2015; Wenegrat & McPhadden 2016*a*,*b*).

Going beyond the basic TTW balance, the influences of density stratification and advective nonlinearity are examined in the SCFT framework. The balanced diagnostic framework is specified for general three-dimensional (3-D) buoyancy b and boundary-layer mixing fields in §§ 2 and 3 the framework is specialized to 2-D configurations for upper-ocean fronts and filaments, which are the particular SCFT problems solved in this paper. Linear TTW SCFT solutions are analysed in § 4 and for comparison comparable solutions are presented in § 5 for the more familiar situation of strain-induced frontogenesis (Hoskins 1982). Nonlinear TTW SCFT solutions with ageostrophic advection are in § 6 and the conclusions are in § 7.

2. Dynamical model

The dynamical starting point is the hydrostatic, incompressible primitive equations (PE) with parameterized surface boundary-layer mixing using the K-profile

parameterization (KPP; Large, McWilliams & Doney 1994; McWilliams, Huckle & Shchepetkin 2009*a*). To allow SCFT comparisons with other effects, an externally imposed barotropic deformation flow aligned with the along-front axis of the geostrophic flow is included. The SCFT model could readily be extended to include the Coriolis frequency gradient β, Wave-averaged Effects of surface gravity waves on the Currents (WEC; Craik & Leibovich 1976; McWilliams, Restrepo & Lane 2004), air–sea coupling expressed through surface wind stress feedbacks and parameterized 3-D frontal instabilities expressed through horizontal eddy diffusion or eddy-induced advection; these generalizations will not be pursued here. Deformation flow is the classical explanation of frontogenesis in the atmospheric literature (Bergeron 1928; Hoskins 1982), and it also is relevant to oceanic surface fronts and filaments (McWilliams, Colas & Molemaker 2009; McWilliams, Molemaker & Olafsdottir 2009*b*). Assume that this deformation axis is in the $\hat{\boldsymbol{y}}$ direction, so that the aligned deformation flow is confluent along this axis, *viz.*

$$u_d = -\partial_y \psi_d = -\alpha x, \quad v_d = \partial_x \psi_d = \alpha y, \quad \psi_d = \alpha xy, \quad \alpha > 0. \tag{2.1a–c}$$

This flow has no horizontal divergence, vertical vorticity or vertical velocity. Its spatially uniform horizontal strain rate is 2α. The governing equations are written in deformation coordinates defined by

$$X = x\mathrm{e}^{\tilde{\beta}}, \quad Y = y\mathrm{e}^{-\tilde{\beta}}, \quad Z = z, \quad T = t, \tag{2.2a–d}$$

where $\tilde{\beta}(t) = \int_0^t \alpha(t')\,\mathrm{d}t'$. The transformed coordinates provide a cogent reference frame for deformation-induced frontogenetic evolution (McWilliams *et al.* 2009*b*). Here, the diagnostic relations will be evaluated instantaneously at $t = 0$ when the $\boldsymbol{\nabla}$ and $\mathrm{D}/\mathrm{D}t$ derivatives can be expressed equivalently in either coordinate system (because $\tilde{\beta} = 0$); hence, the SCFT relations will be expressed with the usual Cartesian notation. Care must be taken with diagnostic relations in the transformed coordinates, and the necessary supporting results are derived in appendix B.

A background resting, stratified state in buoyancy and hydrostatic pressure is indicated by an overbar, which in the problems addressed below can be identified both with a horizontal domain average with the absence of a submesoscale structure in b. Thus, $\partial_z \overline{\phi} = \overline{b}$, where $\phi = p/\rho_0$ is the normalized pressure. The buoyancy and pressure anomalies are indicated by primes, so the total buoyancy field is

$$b = \overline{b} + b'. \tag{2.3}$$

The mean stratification frequency is defined by $N^2(z) = \partial_z \overline{b}$. There is no current associated with this background state.

The analysis perspective is that the coherent flow structures are identified primarily in the buoyancy field b together with the associated hydrostatic dynamic pressure, $\phi = p/\rho_0$, and sea level anomaly η. For idealized flows b will be specified analytically, and from numerical simulations or measurements b will be educed with whatever filtering is needed to remove high-frequency fluctuations such as internal gravity waves. The dynamical maintenance of $\boldsymbol{u}_d$ and $\overline{b}$ is not addressed in this analysis; they merely are assumed as existing and unchanging on the space and time scales relevant to the local flow structures of interest.

For a local buoyancy anomaly b', the associated geostrophic horizontal flow for constant Coriolis frequency f_0 is

$$u_g = -\frac{1}{f_0}\partial_y \phi' = -\partial_y \psi_g, \quad v_g = \frac{1}{f_0}\partial_x \phi' = \partial_x \psi_g, \tag{2.4a,b}$$

and ϕ' is the hydrostatic companion of b', *viz.*

$$\partial_z \phi' = b', \tag{2.5}$$

with $\phi'(0) \approx g\eta$ at the mean level of the upper surface, $z = 0$, and η the surface elevation anomaly. The geostrophic streamfunction is $\psi_g = \phi'/f_0$, which also implies that $b' = f_0 \partial_z \psi_g$.

The 3-D PE system for the local flow anomaly, $\boldsymbol{u}_3 = (\boldsymbol{u}, w)$, relative to $\boldsymbol{u}_d$ is the following:

$$\left.\begin{array}{c} \mathrm{D}[u] - f(y)v = -\partial_x \phi' + \alpha u + \partial_z[\nu_v \partial_z u], \\ \mathrm{D}[v] + f(y)u = -\partial_y \phi' - \alpha v + \partial_z[\nu_v \partial_z v], \\ \partial_z \phi' = b', \\ \mathrm{D}[b'] + N^2 w = \partial_z[\kappa_v \partial_z b]', \\ \boldsymbol{\nabla} \cdot \boldsymbol{u} + \partial_z w = 0. \end{array}\right\} \tag{2.6}$$

Vectors in bold face are 2-D horizontal except when denoted by a subscript 3 for three dimensions. In a β-plane approximation, $f(y) = f_0 + \beta y$. The total horizontal velocity is

$$\boldsymbol{u} = \boldsymbol{u}_g + \boldsymbol{u}_a, \tag{2.7}$$

where the subscript a denotes the ageostrophic component. The substantial derivative is

$$\mathrm{D} = \partial_T + u\mathrm{e}^{\tilde{\beta}} \partial_X + v\mathrm{e}^{-\tilde{\beta}} \partial_Y + w\partial_z; \tag{2.8}$$

as noted above, it is equivalent to the usual Cartesian expression when $t = 0$ and $\tilde{\beta} = 0$. The boundary-layer turbulent vertical mixing coefficients ν_v and κ_v have a specified spatial distribution (e.g. from the KPP scheme).

The surface boundary conditions at $z = 0$ are

$$w(0) = 0, \quad \nu_v \partial_z \boldsymbol{u}(0) = \boldsymbol{\tau}/\rho_0, \quad [\kappa_v \partial_z b]'(0) = \mathcal{B}'. \tag{2.9a–c}$$

A rigid-lid condition is assumed for the diagnosis because the surface w is expected to be small compared to interior w for the submesoscale structures that will be analysed. A further diagnosis of the associated sea level anomaly, $\eta' = \phi'(0)/g$, can be made, and in a time sequence a diagnosis of the associated surface vertical velocity, $w(0) = \mathrm{D}\eta'/\mathrm{D}t$, can be made *post hoc*. Neglecting the contribution of the surface current,

$$\boldsymbol{\tau} \approx \rho_a C_D |\boldsymbol{U}_{atm}| \boldsymbol{U}_{atm} \tag{2.10}$$

is the surface wind stress, where $\boldsymbol{U}_{atm}$ is the near-surface horizontal wind velocity, ρ_a is atmospheric surface density and C_D is the drag coefficient. The surface buoyancy flux anomaly is $\mathcal{B}'$ (note it is not related to maintenance of the background stratification $\bar{b}(z)$). In this paper the focus is on local, upper-oceanic density anomalies and their geostrophic flows that are assumed to vanish in the far field – both in the cross-flow direction (i.e. as $|x| \to \infty$) and with depth (i.e. as $z \to -\infty$ or at $z = -H$) – and to be periodic or invariant in the along-flow direction $\hat{\boldsymbol{y}}$.

This equation set (2.6) and its boundary conditions are commonly the basis for oceanic circulation numerical models. Their general solutions can exhibit great complexity. The SCFT focus will be on particular coherent flow configurations with weak or simple geostrophic advective tendencies because of an aligned or nearly aligned density gradient and geostrophic velocity configuration; e.g. the primary examples below are 2-D fronts or filaments with no geostrophic advective tendency. With a momentum-balanced dynamical approximation for the fluctuations around these basic configurations, diagnostic relations are developed in §§ 2.1–2.2 for the ageostrophic secondary circulation and frontogenetic tendencies (SCFT).

2.1. *Balanced secondary circulation*

To set-up the diagnostic balanced model for $\boldsymbol{u}_{a3} = (\boldsymbol{u}_a, w)$ given $(b, \boldsymbol{u}_g, \boldsymbol{\tau}, \mathcal{B}', \nu_v, \kappa_v)$, the PE system (2.6) is approximated by neglecting ageostrophic acceleration $\partial_t \boldsymbol{u}_a$ in the momentum equations. Many previous proposals for momentum-balanced models have been made (e.g. McWilliams 2003) that suppress inertia–gravity wave behaviour and that have useful higher-order accuracy in Ro compared to the leading-order asymptotic model, quasigeostrophy. Often the alternatives do not give greatly different solutions. In particular, different approximations have been made about which ageostrophic advective terms to include beyond the leading-order geostrophic ones. The approach taken here is the maximalistic approximation of including complete advection in buoyancy and momentum within the hydrostatic constraint. Another distinction is whether the neglected acceleration is ageostrophic ($\partial_t \boldsymbol{u}_a$), as here, or horizontally divergent ($\partial_t \boldsymbol{u}_\chi$, where $\boldsymbol{u}_\chi = \boldsymbol{\nabla}\chi$); because vertical momentum mixing mixes rotational and divergent components of $\boldsymbol{u}$, the former choice is what allows the SCFT model here to be wholly diagnostic. A further simplifying approximation, suitable for submesoscale structures, is an f-plane approximation; i.e. $\beta = 0$. This simplification is not essential for the resulting structure of the diagnostic model.

With the replacement of the pressure gradient force by integration of the hydrostatic balance for b', the SCFT balanced model is

$$\left.\begin{aligned} \mathrm{D}_g[u_g] - f_0(v_g + v_a) + \partial_x \int^z b' \,\mathrm{d}z - \partial_z[\nu_v \partial_z u] &= \mathcal{R}^u, \\ \mathrm{D}_g[v_g] + f_0(u_g + u_a) + \partial_y \int^z b' \,\mathrm{d}z - \partial_z[\nu_v \partial_z v] &= \mathcal{R}^v, \\ \mathrm{D}_g[b'] + N^2 w &= \mathcal{R}^b, \\ \boldsymbol{\nabla}\cdot\boldsymbol{u}_a + \partial_z w &= 0. \end{aligned}\right\} \tag{2.11}$$

The geostrophic substantial derivative is $\mathrm{D}_g = \partial_t + J[\psi_g, \ ]$, with J the horizontal Jacobian operator, $J[p, q] = \partial_x p \partial_y q - \partial_y p \partial_x q$. The left-hand-side terms in (2.11) are those retained in a quasigeostrophic plus Ekman-layer approximation (with vanishing $\boldsymbol{\nabla}\phi'$ at depth), and the right-hand side $\mathcal{R}$ terms collect the residuals of the terms in (2.6) not otherwise written explicitly here; they are defined by

$$\mathcal{R}^u = \mathcal{N}^u + \alpha u, \quad \mathcal{R}^v = \mathcal{N}^v - \alpha v, \quad \mathcal{R}^b = \partial_z[\kappa_v \partial_z b]' + \mathcal{N}^b, \tag{2.12a–c}$$

with the ageostrophic advective nonlinear terms $\mathcal{N}$ defined by

$$\mathcal{N}^{\boldsymbol{u}} = -(\boldsymbol{u}_{a3}\cdot\boldsymbol{\nabla}_3)\boldsymbol{u} - (\boldsymbol{u}_g\cdot\boldsymbol{\nabla})\boldsymbol{u}_a, \quad \mathcal{N}^b = -(\boldsymbol{u}_{a3}\cdot\boldsymbol{\nabla}_3)b'. \tag{2.13a,b}$$

As with (2.6) this system is to be understood as written in deformation coordinates (2.2) but evaluated at $t = 0$ where the metric factors $\exp[\pm\tilde{\beta}]$ in the spatial derivatives are equal to one; this has consequences for further derived relations below.

This balanced dynamical system can, in a familiar way, be separated into an independent prognostic equation for the evolution of its geostrophic streamfunction ψ_g – a generalization of the quasigeostrophic potential vorticity equation with additional right-hand side forcing terms, designated as the balanced potential vorticity equation (BVPE) – and an independent diagnostic equation for its ageostrophic velocity or secondary circulation – the Omega equation ΩE. These two equations, respectively, are defined by the operations BPVE = curl^z [horizontal momentum equations] + $f_0 \partial_z N^{-2}$ [buoyancy equation] and $\Omega\mathrm{E} = f_0 \partial_z$ curl^z [horizontal momentum

equations] $-\nabla^2$ [buoyancy equation]. The formulas for BPVE and ΩE are given in appendix A for completeness. The ΩE operations lead to the cancellation in the $\partial_t \boldsymbol{u}_g$ and $\partial_t b'$ terms from (2.11), showing that ΩE is the consistency condition that assures the equivalence of the ψ_g and b' tendencies in the balanced model. It also may be used as a substitute for the buoyancy equation in (2.11) in comprising a complete dynamical system for determining $\boldsymbol{u}_3$ from b.

The ΩE is central to the SCFT diagnostic approach taken here. However, because of the vertical mixing and ageostrophic advection, this leads here to a generalized 3-D nonlinear Sawyer–Eliassen equation (Eliassen 1962) for $(\boldsymbol{u}_a, w)$ that is fourth order in ∂_z and second order in $\boldsymbol{\nabla}$ with spatially varying coefficients; this can be a difficult operator to invert. A diagnostic Sawyer–Eliassen equation for the secondary circulation in a front or parallel flow or vortex has a long history, in particular in situations of quasigeostrophic or geostrophic momentum balance approximations with specified right-hand side forcings from the geostrophic flow, diabatic heating or eddy momentum flux (e.g. Hoskins & Bretherton 1972).

The present generalization to fully 3-D flows with vertical mixing and nonlinear functional dependency on the ageostrophic flow leads to the alternative SCFT formulation solved here. Because the generalized ΩE is difficult to solve directly, an iterative approach is taken. Furthermore the balanced system (2.11)–(2.13) is split into two subsystems that are each readily solvable at each iteration step. The associated ageostrophic velocity decomposition is designated by

$$\boldsymbol{u}_a = \boldsymbol{u}_T + \boldsymbol{u}_O, \quad w = w_T + w_O, \tag{2.14a,b}$$

with the subscript T denoting the TTW component and O the ΩE component.

The balanced dynamical system is a generalization of conservative geostrophic, hydrostatic dynamics with higher-order validity in Ro and parameterized turbulent vertical mixing. An iterative approach to solving its equations, starting with a geostrophic first evaluation, is likely to succeed if the converged answer is similar in some sense to this first approximation even when Ro is not small (except where balanced solutions do not exist, as can be expected for large Ro; see the discussion at the end of § 2). For upper-ocean submesoscale flow structures that partly occupy the turbulent surface boundary layer, the starting dynamical approximation in the iteration needs to be generalized to include vertical momentum mixing (i.e. TTW). This is the rationale for organizing the iterative solution procedure for (2.11)–(2.13) into the two subsystems defined below by utilizing the flow decomposition (2.14). This partitioned subsystems approach to solving (2.11)–(2.13) is not a unique choice, and other approaches may also be efficacious.

The first subsystem is designated TTW. It is based on the TTW approximation to the left-hand side of the horizontal momentum equation in (2.11). After subtracting out geostrophic balance, the TTW subsystem solves the following equations for $(\boldsymbol{u}_T, w_T)$:

$$\left.\begin{gathered} -\partial_z[\nu_v \partial_z u_T] - f_0 v_T = \partial_z[\nu_v \partial_z u_g] + R^u_T, \\ -\partial_z[\nu_v \partial_z v_T] + f_0 u_T = \partial_z[\nu_v \partial_z v_g] + R^v_T, \\ \boldsymbol{\nabla}\cdot\boldsymbol{u}_T + \partial_z w_T = 0, \\ w_T = 0 \quad \text{and} \quad \nu_v \partial_z \boldsymbol{u}_T = \dfrac{1}{\rho_0}\boldsymbol{\tau} - \nu_v \partial_z \boldsymbol{u}_g + \boldsymbol{Q}_T \quad \text{at } z = 0, \\ \partial_z w_T \quad \text{and} \quad \boldsymbol{u}_T \to 0 \quad \text{as } z \to -\infty. \end{gathered}\right\} \tag{2.15}$$

This is solved in an iterative sequence, $n = 1, 2, \ldots,$ for $(\boldsymbol{u}_T, w_T)^{n+1}$, where the right-hand side terms are evaluated with total $(\boldsymbol{u}, w)^n$ and starting fields of $(\boldsymbol{u}, w)^0 = (\boldsymbol{u}_g, 0)$; their definitions are

$$\left.\begin{array}{c} \mathcal{R}_T^u = \partial_z[\nu_v \partial_z u_O] + \partial_x \mu_g + \mathcal{N}_T^u + \alpha u, \\ \mathcal{R}_T^v = \partial_z[\nu_v \partial_z v_O] + \partial_y \mu_g + \mathcal{N}_T^v - \alpha v, \\ \boldsymbol{\mathcal{Q}}_T = -\nu_v \partial_z \boldsymbol{u}_O(0). \end{array}\right\} \tag{2.16}$$

The field μ_g is the velocity potential for the divergent component of the geostrophic momentum advection in (2.11); it and the ageostrophic advection term $\mathcal{N}_T^{\boldsymbol{u}}$ are defined in (2.18) and (2.19).

The TTW subsystem (2.15)–(2.16) does not contain all the terms in the horizontal momentum equations in (2.11); in particular, it lacks the geostrophic tendency terms $\partial_t \boldsymbol{\nabla}\psi$, and it may be incomplete in its advection terms; this incompleteness will be corrected in the ΩE subsystem (2.20)–(2.21) below.

With $\mathcal{R}_T^{\boldsymbol{u}} = \mathcal{Q}_T = 0$, (2.15) is exactly the simple turbulent thermal wind balance discussed in § 1, and the vertically interiorward values of w_T can be identified with Ekman pumping. The technical advantage of this TTW subsystem is that it fully contains all the vertical momentum mixing terms and thus allows the associated ΩE subsystem (2.20) to be posed as a second-order 3-D elliptic partial differential equation (PDE) problem. The TTW subsystem can be solved as a 1-D linear problem for $\boldsymbol{u}_T$ independently at each (x, y), analogous to solving the Ekman-layer problem with variable $\nu_v(z)$ and specified right-hand side forces. Then w_T is solved from the resulting 3-D $\boldsymbol{u}_T$ field by a simple vertical integration downward from the boundary condition at $z = 0$.

For the system (2.11), there is a constraint on the partition of various terms in the horizontal momentum equations between the TTW and ΩE subsystems. It arises from the fact that TTW solves the horizontal momentum equations, but ΩE only includes information about their curl, hence not about their divergence. In the particular partition defined here this constraint is only relevant for the advection terms. Consider a Helmholtz decomposition of the horizontal vector $\mathcal{N}^{\boldsymbol{u}}$ into its rotational and divergent components,

$$\left.\begin{array}{c} \mathcal{N}^{\boldsymbol{u}} = \mathcal{N}_{div}^{\boldsymbol{u}} + \mathcal{N}_{rot}^{\boldsymbol{u}} = \boldsymbol{\nabla}\mu + \hat{\boldsymbol{z}} \times \boldsymbol{\nabla}\lambda, \\ \nabla^2 \mu = \boldsymbol{\nabla} \cdot \mathcal{N}^{\boldsymbol{u}}, \quad \nabla^2 \lambda = \mathrm{curl}^z[\mathcal{N}^{\boldsymbol{u}}]. \end{array}\right\} \tag{2.17}$$

All of μ must stay in the right-hand side of TTW as μ_T with $\mu_O = 0$, while λ can either partly stay as λ_T or be assigned to ΩE as λ_O, as long as $\lambda = \lambda_T + \lambda_O$. (Because $\nabla^2 \lambda_g$ enters explicitly into ΩE, λ_g itself does not need to be solved for.) For the SCFT applications in this paper, the choice is made separately (i) for the geostrophic advection,

$$\nabla^2 \mu_g = 2J[\partial_x \psi_g, \partial_y \psi_g], \quad \nabla^2 \lambda_g = -J[\psi_g, \nabla^2 \psi_g], \tag{2.18a,b}$$

which are assigned to TTW and ΩE, respectively, so that they occupy their usual positions in quasigeostrophic theory, and (ii) for the ageostrophic advection, which is wholly assigned to μ_T and λ_T; i.e. $\mu_O = \lambda_O = 0$, and

$$\mathcal{N}_T^{\boldsymbol{u}} = \mathcal{N}^{\boldsymbol{u}}, \tag{2.19}$$

where the right-hand side is specified in (2.13). For SCFT problems with additional dynamical effects represented in $\mathcal{R}^{\boldsymbol{u}}$, a similar constraint must be respected. For 2-D

fronts and filaments, the geostrophic momentum advection is zero, $\mu_g = \lambda_g = \mathcal{N}_O^{\boldsymbol{u}} = 0$ (§ 3).

The ΩE subsystem is derived by the previously indicated operation on (2.11), whose result is in appendix A, and by subtracting the terms already contained within the TTW subsystem. It solves the following equations for $(\boldsymbol{u}_O,\ w_O)^{n+1}$ after the solution of the TTW subsystem at $n+1$:

$$\left.\begin{aligned} [f_0^2\partial_z^2 + N^2(z)\nabla^2]w_O &= -2f_0\boldsymbol{\nabla}\cdot J[\boldsymbol{\nabla}\psi_g,\ \partial_z\psi_g] - N^2(z)\nabla^2 w_T, \\ &\quad + \alpha(\partial_{xx}b' - \partial_{yy}b') + \mathcal{N}_O^{\Omega} + \nabla^2\partial_z[\kappa_v\partial_z b]', \\ \boldsymbol{\nabla}\cdot\boldsymbol{u}_O + \partial_z w_O &= 0, \\ w_O &= 0 \quad \text{at } z = 0, \\ w_O \to -w_T \quad &\text{as } z \to -\infty \quad \text{or} \quad \text{at } z = -H, \\ w_O \to 0 \quad &\text{in horizontal far field or is periodic,} \end{aligned}\right\} \tag{2.20}$$

where

$$\left.\begin{aligned} \mathcal{N}_O^{\boldsymbol{u}} &= \hat{\boldsymbol{z}}\times\boldsymbol{\nabla}\lambda_g, \\ \mathcal{N}_O^{b} &= -(\boldsymbol{u}_{a3}\cdot\boldsymbol{\nabla}_3)b', \\ \mathcal{N}_O^{\Omega} &= -f_0\partial_z\,\mathrm{curl}^z[\mathcal{N}_O^{\boldsymbol{u}}] + \nabla^2\mathcal{N}_O^{b}. \end{aligned}\right\} \tag{2.21}$$

The right-hand side terms are evaluated using $(\boldsymbol{u}_T,\ w_T)^{n+1}$ and $(\boldsymbol{u}_O,\ w_O)^n$. The geostrophic acceleration from momentum has been cancelled by the buoyancy tendency, the geostrophic momentum advection has been combined with the geostrophic buoyancy advection to form the first right-hand side term and the term $f_0^2\partial_z^2 w_T$ has been cancelled as part of the subtracted TTW subsystem balance. The derivation of the right-hand side α term is in appendix B. This subsystem is a 3-D linear, second-order elliptic problem for w_O with independent 2-D Poisson equation problems for $\boldsymbol{u}_O = \boldsymbol{\nabla}\chi_O$ and $\nabla^2\chi_O = -\partial_z w_O$ at each z. The left-hand side operator inversion will be well behaved as long as $N^2 > 0$. With $\mathcal{N}^{\Omega} = 0$, it is equivalent to the quasigeostrophic ΩE; however, notice that even in this simple quasigeostrophic case w_O imposes a correction on w_T that expresses the suppressive effect on vertical motion of the stable stratification N^2 in the oceanic interior. By comparison with (A 3)–(A 4), the composition of (2.20)–(2.21) can be recognized after the subtraction of the TTW subsystem balances.

A flow chart of the solution procedure is thus the following: given b, $(\nu_v,\ \kappa_v)$, and $(\boldsymbol{\tau},\ \mathcal{B})$, $\boldsymbol{u}_g$ is obtained from (2.4), then in an iterative sequence, $(\boldsymbol{u}_a,\ w)$ are obtained from the TTW subsystem for $(\boldsymbol{u}_T,\ w_T)$ and the ΩE subsystem for $(\boldsymbol{u}_O,\ w_O)$. With a convergence of the iteration sequences, this yields a complete solution of the balanced system (2.11). The experience in obtaining the SCFT solutions in this paper is that convergence is readily achieved in most situations, barring excessively large Ro_g values; near the convergence limit small values of γ in (2.24) can be helpful.

The general $\mathcal{R}$ formulations in (2.12)–(2.13), (2.16) and (2.21) are seemingly complicated, but the explanatory utility of a SCFT analysis will be greatest in particular idealized situations where the $\mathcal{R}$ forms are simpler (e.g. for 2-D $b(x,\ z)$ in § 3). As with most balanced models, there is no guarantee of solution existence for finite Ro; in particular, when the geostrophic advective tendencies are zero for a coherent structure, finite Ro is a measure of the magnitude of ageostrophic advection (§ 6).

In more general evolutionary dynamics, e.g. the full PE (2.6), a failure of balance would manifest itself with an outbreak of faster oscillations and/or smaller

spatial scales. Non-existence of a balanced solution would be manifested here as non-convergence of the TTW + ΩE iteration cycle, although non-convergence does not necessarily imply non-existence. In this paper the limits of convergence will be approached but not probed assiduously. In some approximate balanced models, the solvability conditions can be identified analytically (e.g. McWilliams *et al.* 1998), but that is not readily accomplished in the present situation with vertical mixing. Furthermore, experience with circulation models (e.g. Gula *et al.* 2014; Sullivan & McWilliams 2016; Suzuki *et al.* 2016) indicates that often, even at quite large Ro, the simulated secondary circulations and frontogenesis in fronts and filaments are qualitatively similar to the solutions shown below, suggesting that their dynamics can remain close to, even if not exactly, balanced. The present paper provides an analytic basis for the balanced SCFT when $Ro \sim 1$, but as yet there is no such basis for the phenomenologically similar behaviours at $Ro \gg 1$.

Finally, it should be understood that these diagnostic solutions for $\boldsymbol{u}_3$, given b, are not steady in time. Rather, they have nonzero time derivatives that have been minimized by the selection of appropriate 'coherent-structure' spatial configurations for b and by the balance approximations in the TTW + ΩE system that both preclude inertia–gravity wave dynamics and incorporate much of the advective tendency in cancellation with other tendency terms. (In a weather forecasting context this would be called an initialization procedure.) Given the SCFT solution, the tendencies for $\boldsymbol{u}_g$ and b can be evaluated in (A 1) and (2.11), as can the frontogenetic tendencies in § 2.2.

2.2. *Frontogenetic tendency*

A complementary diagnostic perspective comes from evaluating the buoyancy gradient tendency associated with the diagnosed secondary circulation. The frontogenetic tendency equation is formed by taking the horizontal derivative of the buoyancy equation in (2.6) and then taking its dot product with $\boldsymbol{\nabla} b'$. Again, the derivation is made in the deformation-following transformed coordinates, and the result is expressed in Cartesian coordinates (appendix B):

$$\begin{aligned} \mathrm{D}[\tfrac{1}{2}(\boldsymbol{\nabla} b')^2] \;&=\; -f^2 \boldsymbol{\nabla} \partial_z \psi_g \cdot J[\boldsymbol{\nabla}\psi_g, \partial_z \psi_g] - N^2 \boldsymbol{\nabla} w \cdot \boldsymbol{\nabla} b' - [\boldsymbol{\nabla} b' \cdot \boldsymbol{\nabla}](\boldsymbol{u}_{a3}) \cdot \boldsymbol{\nabla}_3 b \\ &\quad + \alpha((\partial_x b')^2 - (\partial_y b')^2) + [\boldsymbol{\nabla} b' \cdot \boldsymbol{\nabla}]\partial_z(\kappa_v \partial_z b) \\ &=\; \mathcal{T}^b = \mathcal{T}^b_g + \mathcal{T}^b_{adv} + \mathcal{T}^b_\alpha + \mathcal{T}^b_{\kappa_v}. \end{aligned} \tag{2.22}$$

These tendency terms, respectively, are the geostrophic self-straining $\mathcal{T}^b_g$, two ageostrophic horizontal strain terms associated with buoyancy advection combined in $\mathcal{T}^b_{adv}$, external straining deformation $\mathcal{T}^b_\alpha$, and boundary-layer vertical buoyancy mixing $\mathcal{T}^b_{\kappa_v}$. The final line indicates the notation for each of these right-hand side terms. All of them are known from the geostrophic flow and the secondary-circulation solution of the TTW + ΩE system in the preceding section. The interpretation is that the right-hand side terms indicate the rate of change in $(\boldsymbol{\nabla} b)^2/2$ in a Lagrangian reference frame. They have no time derivatives; i.e. their evaluation is diagnostic. Positive right-hand side terms in (2.22) indicate a frontogenetic tendency.

In McWilliams *et al.* (2009*b*), the frontogenetic tendency effects were diagnostically evaluated in Cartesian coordinates without explicitly implicating the external strain α frontogenesis effect. The results there are not wrong, but this neglect of showing the dominant frontogenetic tendency effect explicitly is regrettable in retrospect. The derivation of this α term is in appendix B.

An analogous diagnostic equation can be derived for the tendency in horizontal shear variance, $(\boldsymbol{\nabla u})^2$. In some cases (e.g. a dense filament; McWilliams *et al.* 2015), this perspective is more informative about the subsequent frontogenetic evolution than is the buoyancy tendency (2.22). By operating on the horizontal momentum equation j in (2.6) with $(\partial_i u^j)\partial_i$, the following frontogenetic tendency relation is obtained:

$$\begin{aligned} \mathrm{D}[\tfrac{1}{2}(\partial_i u^j)(\partial_i u^j)] \;&=\; -(\partial_i u^j)(\partial_i \partial_j \phi') - (\partial_i u^j)(\partial_i u^k)(\partial_k u^j) \\ &\quad - (\partial_i u^j)(\partial_i w)(\partial_z u^j) + 2\alpha((\partial_x u)^2 - (\partial_y v)^2) \\ &\quad + (\partial_i u^j)\partial_i \partial_z [\nu_v \partial_z u^j] \\ &=\; \mathcal{T}^{\boldsymbol{u}} = \mathcal{T}^{\boldsymbol{u}}_{\phi} + \mathcal{T}^{\boldsymbol{u}}_{adv} + \mathcal{T}^{\boldsymbol{u}}_{\alpha} + \mathcal{T}^{\boldsymbol{u}}_{\nu_v}. \end{aligned} \tag{2.23}$$

A horizontal index notation ($i, j, k = 1, 2$) is used with repetition implying summation. The notation ∂_i is a shorthand for the partial derivative with respect to x^i, and u^k is the kth component of $\boldsymbol{u}$. The tendency terms are due to, respectively, pressure gradient, horizontal and vertical advection, external deformation, and boundary-layer vertical momentum mixing. The derivation of $\mathcal{T}^{\boldsymbol{u}}_{\alpha}$ is in appendix B. No approximation to (2.6) is made here other than $\beta = 0$; i.e. the left-hand side of (2.23) formally includes the total acceleration. Even in 3-D flows, there is no contribution to $\mathcal{T}^{\boldsymbol{u}}_{adv}$ and $\mathcal{T}^{\boldsymbol{u}}_{\phi}$ from wholly $\boldsymbol{u}_g$ terms.

2.3. *Numerical methods*

A numerical solution method is developed to solve the TTW + ΩE subsystems iteratively (§ 2.1) and then to evaluate the diagnostic frontogenetic tendencies (§ 2.2) and buoyancy fluxes (§ 3). It is based on a uniform spatial grid in x and y and a stretched, staggered grid in z, with (u, v, b) at cell centres and (w, N^2) at cell edges and finer resolution near the surface. The differential operators are discretized with second-order accuracy. The elliptic operators are solved by matrix inversion. Iteration convergence is accelerated by relaxation, e.g.

$$\gamma w^{n+1} + (1-\gamma) w^n \;\longrightarrow\; w^{n+1} \tag{2.24}$$

for $\gamma \leqslant 1$, after each solution cycle in the TTW and ΩE subsystems.

The fields $b(\boldsymbol{x}_3)$, $\nu_v(\boldsymbol{x}_3)$ and $\kappa_v(\boldsymbol{x}_3)$ are specified analytically and particular numerical parameters are listed in § 3.2.

3. Two-dimensional fronts and filaments with surface wind stress

The particular idealized situations of interest here are submesoscale fronts and filaments in the upper ocean that are uniform in y. Surface wind stress is included, hence there is a vertical mixing in the turbulent boundary layer above $z = -h(x)$.

3.1. *Two-dimensional SCFT equations*

For this problem the TTW + ΩE system (2.15)–(2.21) in § 2.1 is greatly simplified. The along-axis derivative is zero, $\partial_y = 0$. The only geostrophic flow is $v_g = \partial_x \psi_g$ and the vertical vorticity is $\zeta = \partial_x v_T$. There is no geostrophic advection; thus, $\mu_g = \lambda_g = J[\psi_g, b'] = 0$. Ageostrophic advection is only in the cross-axis plane: $D = \partial_t + u\partial_x + w\partial_z$. With these simplifications the 2-D forms of the TTW, ΩE, $\mathcal{T}^b$ and $\mathcal{T}^{\boldsymbol{u}}$ equations are listed in appendix C.

Because the frontal spatial scale is small, the wind stress $\boldsymbol{\tau}$ is assumed to be spatially uniform. The focus is on the interplay among wind stress, the boundary-layer

vertical mixing, and the submesoscale structure in $b(x, z)$. Thus, any consideration of surface buoyancy flux forcing effects is deferred: $\mathcal{B}'$ is set to zero, and $\kappa_v(x, z) \approx \nu_v(x, z)$, as in the KPP scheme. However, oceanic circulation models (Gula *et al.* 2014) and large eddy simulations with resolved boundary-layer turbulence (Sullivan & McWilliams 2016) show similar SCFT behaviours with convective $\mathcal{B}'$ for the essential reason that the turbulence, no matter how it is generated, causes vertical momentum mixing which in turn causes a frontogenetic secondary circulation for a front or filament. Nagai *et al.* (2006) analyses frontal secondary circulations when $\kappa_v \neq \nu_v$.

The bottom of the domain is at $z = -H$, which is much deeper than the boundary-layer depth at $z = -h(x)$.

3.2. *Analytic formulas for b', ν_v and κ_v*

The buoyancy field for a straight (2-D), upper-ocean front or filament is idealized as

$$b(x, z) = b_0 + N_b^2(z + H) + \frac{N_0^2}{2}[(1 + \Gamma)z - (1 - \Gamma)(h(x) + \lambda^{-1} \log \cosh[\lambda(z - \eta + h(x))])]. \quad (3.1)$$

The square of the buoyancy frequency for the interior stratification is N_0^2, and N_0^2 is a weak background minimum stratification ($0 < N_b^2 \ll N_0^2$) that assures that $\partial_z b$ is positive everywhere. The fractional reduction of the surface boundary-layer stratification (relative to the interior N_0^2) is Γ (i.e. $0 \leqslant \Gamma \ll 1$). The vertical scale of the transition between these two regimes λ^{-1} occurs around the base of the boundary layer at $z = -h(x)$. The upper free surface is at $z = \eta(x)$, with $\eta \ll h$. The surface elevation is evaluated by vertical integration of hydrostatic balance, $\partial_z \phi = b$, upward from $z = -H$ where $\partial_x \phi' = \partial_x b' = 0$ to reach the surface boundary condition of a constant (atmospheric) value of ϕ at $z = \eta(x)$; equivalently, $\phi'(x, 0) \approx g\eta(x)$ by linearizing this surface pressure condition about $z = 0$.

The distinction between a front or filament is determined by the choice of $h(x)$, i.e. a step in the former case and a localized extremum in the latter. For a front the choice is

$$h_{fr}(x) = h_0 - \frac{\delta h}{2} \operatorname{erf}\left[\frac{x}{\ell}\right], \quad (3.2)$$

with $x = 0$ the centre of the front, ℓ the half-width, h_0 the central depth and δh the depth change across the front. For $\delta h > 0$, the deep side of the frontal mixed layer is $x < 0$ (west), which therefore is also the dense side in (3.1). The relation between the surface buoyancy horizontal change across the front δb_s and δh from (3.1) is

$$\delta b_s \approx -(1 - \Gamma)N_0^2 \delta h. \quad (3.3)$$

In the far fields at depth and on either side, h_{fr} goes to $h_0 \pm (\delta h)/2$ and $b(z)$ goes to two different horizontally uniform stratification profiles. With $f_0 > 0$ the associated geostrophic velocity v_g is a northward surface jet around the front centre, mostly confined to the weakly stratified upper layer, with equal cyclonic and anti-cyclonic vorticity extrema on the west (dense) and east (light) sides, respectively. An analogous dense surface filament has

$$h_{df}(x) = h_0 + \delta h \exp\left[-\left(\frac{x}{\ell}\right)^2\right]. \quad (3.4)$$

Its surface buoyancy anomaly δb_s is again given by (3.3), and its $v_g(x, z)$ is a double jet, with $v_g > 0$ on the east side and a dominant cyclonic $\zeta_g = \partial_x v_g > 0$ in the centre

with weaker negative lobes on the sides. A light surface filament would occur for (3.4) with $\delta h < 0$; it has a weaker strain-induced frontogenesis rate (McWilliams *et al.* 2009) and is thought to be rarer and/or weaker in nature and simulations; so the focus will be on dense filaments.

In association with the particular $h(x)$ shape functions in (3.2) and (3.4), the maximum values at the surface for the geostrophic along-axis velocity and vorticity are

$$V_g \approx C_v \frac{h_0 \delta b_s}{f_0 \ell} \quad \text{and} \quad \max\left[\frac{\zeta_g}{f_0}\right] \approx C_\zeta \frac{h_0 \delta b_s}{(f_0 \ell)^2}, \tag{3.5a,b}$$

with geometric shape coefficients $C_v = 0.5$ and 1.0 and $C_\zeta = 0.5$ and 2.4, respectively, for the analytic formulas (3.2) and (3.4) for the front and dense filament. From these relations and (3.3), the strength of a submesoscale flow and its geostrophic Rossby number, $Ro_g = \zeta_g/f_0$, increase with the following influences: a stronger surface density anomaly δb_s (which in turn increases with stronger interior stratification N_0 and boundary-layer depth anomaly δh); lower latitude f_0; deeper boundary-layer depth h_0; and smaller horizontal width ℓ (i.e. deeper within the submesoscale range). In particular, if such flow structures are formed by frontogenetic processes that decrease ℓ while holding these other quantities approximately constant, then v_g and Ro_g will increase as the frontogenesis proceeds.

The variation in $h(x)$ implies a variation in the vertical mixing if h is interpreted as the boundary-layer depth. A KPP prescription (Large *et al.* 1994) for the vertical eddy viscosity in a wind-driven boundary layer is

$$\left.\begin{aligned} \nu_v(x,z) &= k u_* h(x) \mathcal{G}(\sigma) + \nu_{v0}, \quad \sigma = -\frac{z}{h}, \\ \mathcal{G} &= \frac{(\sigma+\sigma_0)(1-\sigma)^2}{(1+\sigma_0)^2} \quad \text{if } \sigma \leqslant 1, \\ \mathcal{G} &= 0 \quad \text{if } \sigma > 1. \end{aligned}\right\} \tag{3.6}$$

The von Kármán constant is $k = 0.4$; $u_* = \sqrt{|\tau|/\rho_0}$ is the oceanic wind-friction velocity; σ is a normalized depth coordinate, and $\sigma_0 = 0.005$ is a velocity logarithmic singularity regularization constant as $\sigma \to 0$; and ν_{v0} is a small interior background eddy viscosity. In the absence of surface buoyancy flux ($\mathcal{B}' = 0$), $\kappa_v \approx \nu_v$ in the boundary layer, but usually $\kappa_{v0} \leqslant \nu_{v0}$ in the interior. This is a reduced version of KPP by including only its dependencies on b and the surface wind stress. A more complete version would depend also on $\boldsymbol{u}$, but that would complicate the analysis here; furthermore, as yet not much is known about how vertical mixing might change inside a submesoscale flow structure.

For purposes of illustration a standard set of parameter values is used:

$$\left.\begin{aligned} &f_0 = 0.78 \times 10^{-4}\ \text{s}^{-1}, \quad h_0 = 60\ \text{m}, \quad \delta h = 15\ \text{m}, \quad N_0^2 = 3.4 \times 10^{-5}\ \text{s}^{-2}, \\ &N_b^2 = 1.0 \times 10^{-7}\ \text{s}^{-2}, \quad b_0 = 6.4 \times 10^{-3}\ \text{m s}^{-2}, \quad \Gamma = 0.025, \quad \lambda^{-1} = 3\ \text{m}, \\ &\nu_{v0} = 1.0 \times 10^{-4}\ \text{m}^2\ \text{s}^{-1}, \quad u_* = 0.01\ \text{m s}^{-1}, \quad \sigma_0 = 5 \times 10^{-3}, \quad H = 250\ \text{m}. \end{aligned}\right\} \tag{3.7}$$

Most of these parameters are defined in the formulas (3.1), (3.2), (3.4) and (3.6). This u_* value corresponds to an atmospheric surface wind speed of $U_{atm} = 8.2$ m s^{-1} under neutral stratification conditions in (2.10); its direction is θ_τ, with the convention that it increases counter-clockwise from an origin in the east direction. To have roughly comparable δb_s, maximum v_g, and maximum ζ_g values, widths of $\ell = 1.5$ km for the

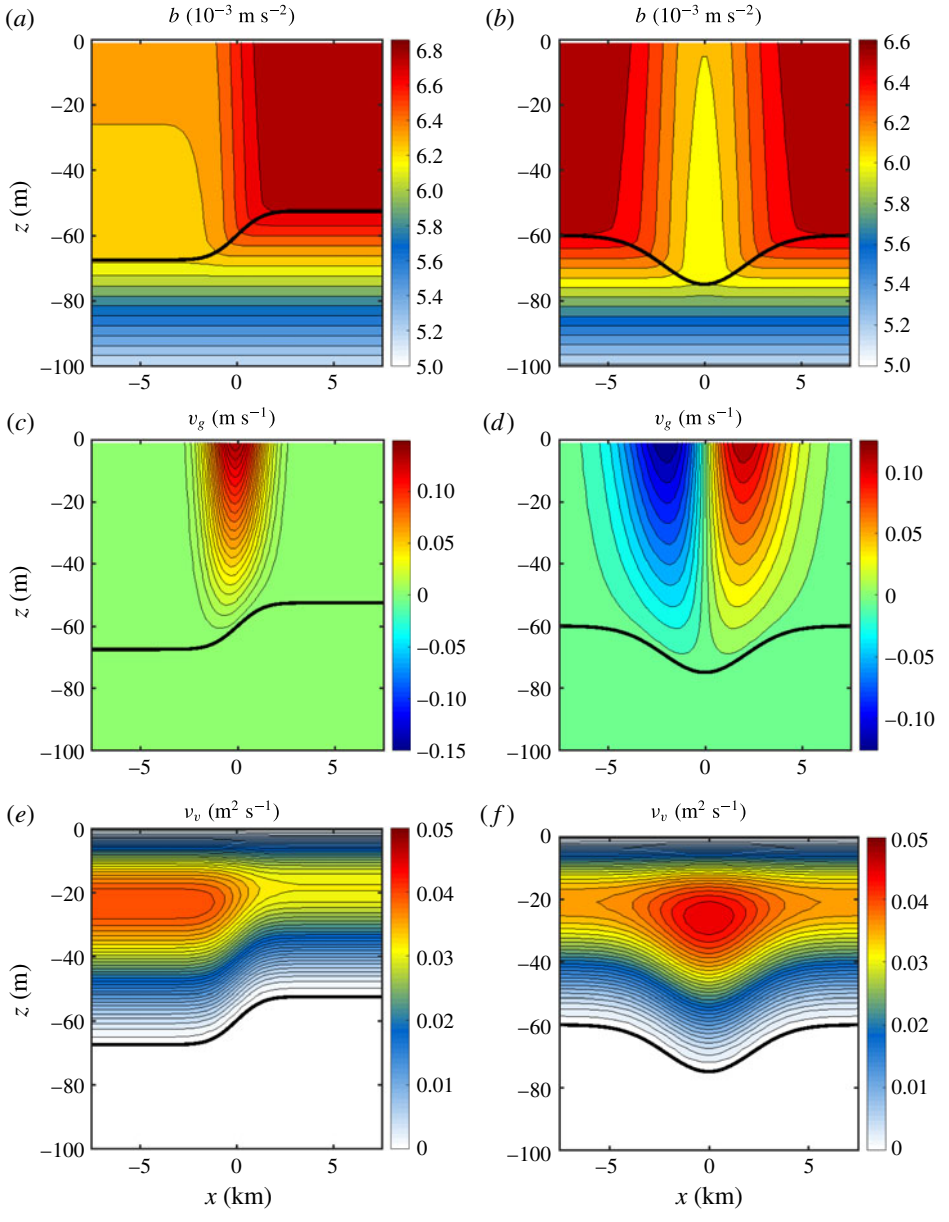

FIGURE 1. Idealized shapes for a 2-D front (*a*,*c*,*e*) and dense filament (*b*,*d*,*f*) with (3.1), (3.2), (3.4) and (3.7): $b(x, z)$ (*a*,*b*), $v_g(x, z)$ (*c*,*d*) and $\nu_v(x, z)$ (*e*,*f*). The boundary-layer depth $z = -h(x)$ is indicated by the thick black line. Only a portion of the full domain is plotted. The δb_s values here correspond to a surface temperature difference of 0.25 °C with a thermal expansion coefficient of $\alpha^* \approx 2 \times 10^{-4}$ K^{-1}.

front and $\ell = 3$ km for the dense filament are chosen. The corresponding buoyancy, geostrophic velocity and eddy viscosity fields are shown in figure 1. These parameter values represent a mid-sized submesoscale surface front or filament, rather than, e.g. a mesoscale flow structure with a larger ℓ and a deeper reach below the surface layer.

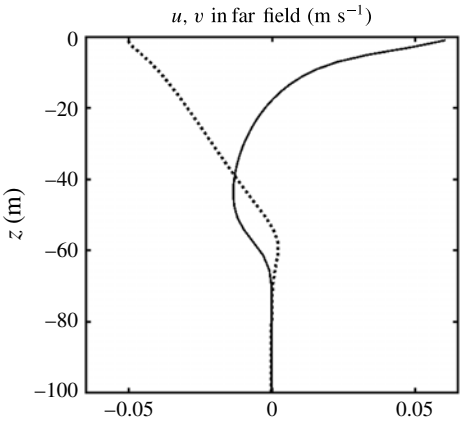

FIGURE 2. Vertical profiles of horizontal velocity in the far-field Ekman layer $\boldsymbol{u}_\infty(z)$ for a dense filament with $\theta_\tau = 0$ (i.e. eastward wind). The solid line is $u_\infty(z)$, and $v_\infty(z)$ is dotted. The velocity shear is high at the top and bottom of the layer where $\nu_v(z)$ is small.

For the solutions reported in this paper, the discrete calculations are made with a horizontal grid size of $\mathrm{d}x = 0.24$ km and a stretched vertical grid with $\mathrm{d}z = 2$ m near the surface. This seems adequate to resolve the solution structure except perhaps for strong nonlinearity near the limit of TTW + ΩE system convergence when some flow structures become horizontally narrow (§ 6).

3.3. *Buoyancy flux*

Another diagnostic for the solutions below is the integrated buoyancy flux. For a 2-D $b(x, z)$, vertical and horizontal fluxes are defined by

$$BF_v(z) = \int_{-L_x/2}^{L_x/2} w'b' \,\mathrm{d}x, \quad BF_h(x) = \int_{-H}^{0} ub' \,\mathrm{d}z, \tag{3.8a,b}$$

where the prime denotes the deviation from the average value in the x far field. Because $\overline{w} = 0$ in almost all the SCFT solutions below, w' is usually the total vertical velocity. (An exception is for a front when U_{atm} is very large, discussed at the end of § 4.2; BF_v is not analysed in this case.) The total u is retained in BF_h because $\overline{u}$ is typically non-zero when $u_* \neq 0$, and the far-field velocity in x is the Ekman current. The horizontal domain width L_x is chosen to be much larger than ℓ.

4. Linear TTW solutions

In this section consider the 2-D problems in the TTW + ΩE system posed in §§ 2.1 and 3 with $\mathcal{N}^{\boldsymbol{u}} = \mathcal{N}^b = 0$.

4.1. *Far-field velocity*

The TTW subsystem solution in the far field where $\partial_x b$ vanishes is simply an Ekman-layer velocity profile $\boldsymbol{u}_\infty(z)$ (e.g. figure 2), and ΩE adds no correction. Because it is independent of x, it has no associated w or BF_v, and it is uninfluenced by advection even when $\mathcal{N}^{\boldsymbol{u}}, \mathcal{N}^b \neq 0$. It has the expected attributes known from constant-ν solutions:

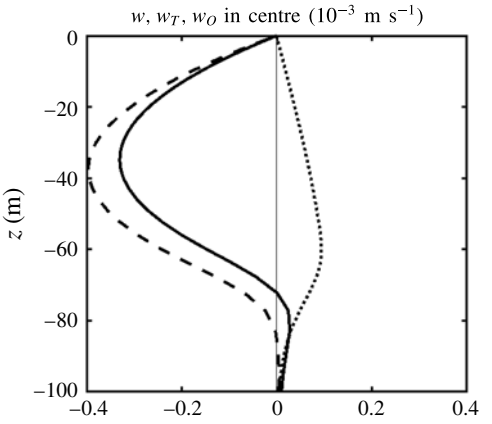

FIGURE 3. Linear TTW vertical velocity decomposition in the downwelling branch located at the centre of a dense filament ($x = 0$) with the same parameters as in figure 4, where $w(x, z)$ is shown. Here $w = w_T + w_O$ with w solid, w_T dashed and w_O dotted. In this solution the Ekman pumping is zero, $w_{ek} = 0$.

the surface current is rotated anti-cyclonically (clockwise for $f > 0$) from the surface stress, and with depth it rotates further in this direction while decreasing in amplitude. Its depth-integrated ageostrophic horizontal transport is

$$\boldsymbol{T}_T = \int_{-\infty}^{0} \boldsymbol{u}_T(z')\,\mathrm{d}z' = \hat{\boldsymbol{z}} \times \frac{\boldsymbol{\tau}}{f\rho_0}. \tag{4.1}$$

With the variable eddy viscosity ν_v profile in (3.6), these same attributes still occur, but the profile shape is altered with increased vertical shear at the top and bottom of the $[-h, 0]$ layer where ν_v becomes small. The anti-cyclonic rotation angle at the surface is smaller, and $\boldsymbol{u} \approx 0$ for $z \leqslant -h$. A scaling estimate for the Ekman current based on (4.1) is

$$V_{ek} = \frac{u_*^2}{f_0 h_0}, \tag{4.2}$$

which is representative of the mid-layer speed, with the surface value approximately twice larger. With changing wind direction θ_τ, the $\boldsymbol{u}_\infty(z)$ profile is unchanged except for a rotation with θ_τ.

4.2. *Secondary circulation*

The velocity decomposition (2.14) represents the primary TTW solution ($\boldsymbol{u}_T$, w_T) due to the wind stress, buoyancy gradient and vertical momentum mixing. The ΩE correction ($\boldsymbol{u}_O$, w_O) is due to the stratification and vertical buoyancy mixing, with an iteration between them for dynamical consistency. Figure 3 shows that overall w is close to w_T in this linear dense filament solution, but the w_O correction is not trivial, especially near the bottom of the surface layer where the stratification begins to increase. At depth, the cancellation between w_T and w_O is complete, and w is zero below. (In figure 3 this cancellation is only slightly evident because all w components are vanishing near the bottom of the surface layer, but in § 6 ageostrophic advection causes $w_T = -w_O \neq 0$ to extend to the bottom of the domain.)

A vertical integral of the momentum equations in (2.15) with $\mathcal{N}_T^{\boldsymbol{u}} = 0$ shows that the ageostrophic transport relation (2.15) for $\boldsymbol{T}_T$ is unaltered by the presence of $b(x, z)$ and

$\nu_v(x, z)$, so there can be no Ekman pumping even in the near field of the submesoscale structure, i.e. $w_{ek} \approx \partial_x T^x_T = 0$ (neglecting a small contribution from $u(x, -h)\partial_x h$ because $u(x, -h)$ is small). This restricts the vertical velocity to the surface layer in this linear TTW case.

The associated ageostrophic secondary circulation for a dense filament is shown in figure 4. The horizontal components are defined by

$$\boldsymbol{u}'_a(x, z) = \boldsymbol{u}(x, z) - \boldsymbol{u}_g(x, z) - \boldsymbol{u}_\infty(z), \tag{4.3}$$

where the prime again denotes a departure from the far-field average. The circulation in the (x, z) plane consists of two counter-rotating cells. Because the velocity is 2-D incompressible, this circulation can be expressed with an overturning streamfunction $\Phi(x, z)$ defined by

$$u'_a = \partial_z \Phi \quad \text{and} \quad w = -\partial_x \Phi. \tag{4.4a,b}$$

The total circulation is $(u'_a, w)(x, z)$ plus the far field $u_\infty(z)$ (figure 2). The central downwelling jet is stronger than the peripheral upwelling flows. In the along-front direction, $v'_a(x, z)$ mirrors $u'_a(x, z)$ in its spatial pattern; relative to $v_g(x, z)$ (figure 1*d*), it reduces the geostrophic shear by weakening v in the upper part of the boundary layer and strengthening it in the lower part. It also reduces the vertical vorticity in the filament; the peak value for ζ_g/f is 1.33 and the reduced peak for ζ/f is 0.99 (not shown). Note that these normalized values comprise a Ro, and the values are not small here, as for many submesoscale flows.

This orientation relationship between $\boldsymbol{u}'_a(z)$ and $\boldsymbol{u}_g(z)$ holds at each horizontal location in the TTW subsystem with only modest adjustments from the ΩE subsystem, and it is nearly independent of $\boldsymbol{\tau}$ when $\boldsymbol{\nabla} b$ is as relatively large as it is here (but see figures 6 and 7 below). Figure 5 shows these velocity profiles in the centre of the northward along-front jet. The surface ageostrophic flow is rotated cyclonically by an obtuse angle relative to the surface geostrophic shear and it reverses in the lower part of the boundary layer.

In the TTW + ΩE system there are two external drivers to the circulation, $\boldsymbol{\tau}$ and $\boldsymbol{\nabla} b$. To assess their relative importance in figures 4 and 8, artificial alternative solutions are obtained by setting $\boldsymbol{\tau} = 0$, while retaining ν_v, κ_v as before. The results (not shown) are TTW circulations that are visually nearly indistinguishable from ones with $\boldsymbol{\tau} \neq 0$, except that now $\boldsymbol{u}_\infty = 0$. This is consistent with the fact that the secondary circulation is nearly independent of θ_τ for the parameter values (3.7).

A scaling estimate for the TTW secondary circulation comes from a primary balance in the y-momentum equation in (2.15),

$$f_0 u'_a \sim \partial_z(\nu_v \partial_z v_g) \sim \frac{\nu_{v\infty} \max[|\partial_x b|]}{f_0 h_0} \quad \text{and} \quad u'_a \sim \partial_z \Phi \sim \frac{\Phi}{h_0}, \tag{4.5a,b}$$

where the far-field values are used for ν_v and h and the maximum value of $\partial_x b$ is used for the buoyancy gradient. This leads to a scaling estimate,

$$\Phi_{ttw} = \frac{\nu_{v\,max} \max[|\partial_x b|]}{f_0^2}, \tag{4.6}$$

where, from (2.10) and (3.7),

$$\nu_{v\,max} = 0.061 u_* h_0 = 7.5 \times 10^{-5} |\boldsymbol{U}_{atm}| h_0. \tag{4.7}$$

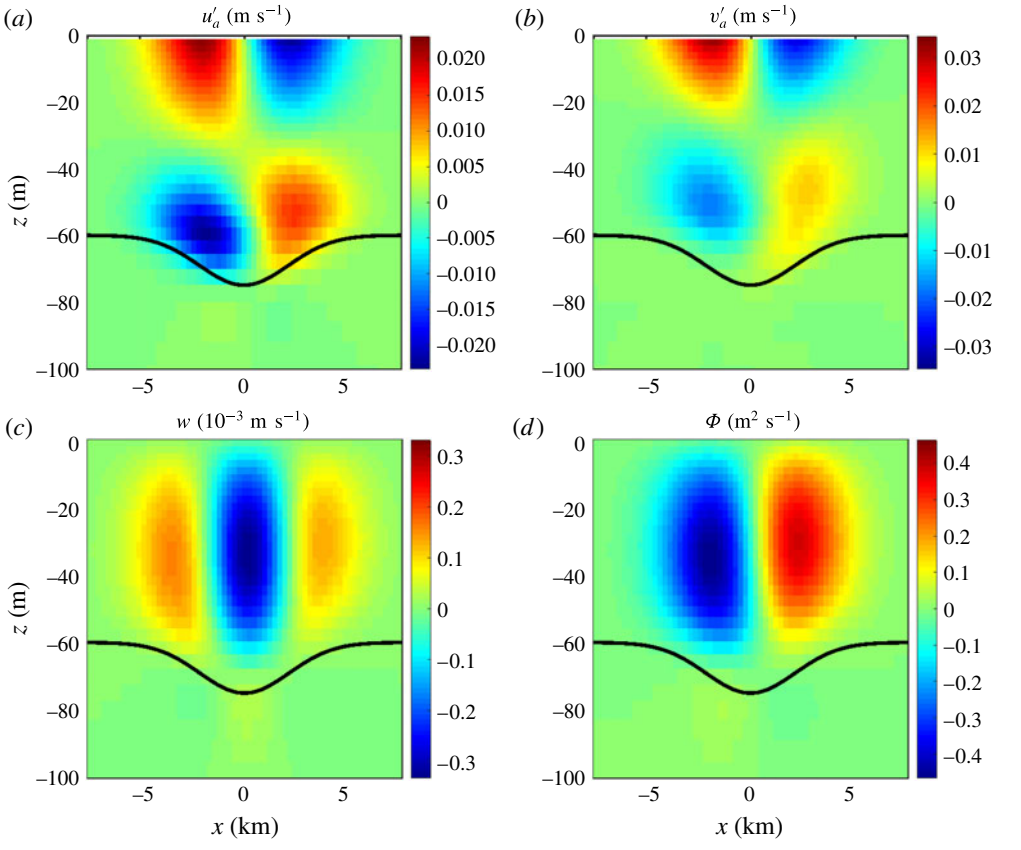

FIGURE 4. Linear TTW secondary circulation for a dense filament with $\theta_\tau = 0$: (*a*,*b*) u'_a and v'_a after subtracting the far field $\boldsymbol{u}_\infty(z)$ in figure 2 and (*c*,*d*) w and Φ. The accompanying b, v_g, v_v fields are in figure 1(*b*,*d*). Again and throughout the paper, $z = -h(x)$ is indicated by the thick black line.

(The subscript *ttw* here is meant to distinguish a particular dynamical balance that is close to simple turbulent thermal wind from the velocity decomposition (2.14), where T denotes the solution of the TTW subsystem (2.15) that can be valid for a much wider range of dynamical balances.) Thus, using (3.5), the TTW scaling estimates are

$$\Phi_{ttw} = 0.1\frac{u_* V_g}{f_0}, \quad V_{ttw} = 0.1\frac{u_* V_g}{f_0 h_0}, \quad W_{ttw} = 0.1\frac{u_* V_g}{f_0 \ell}. \tag{4.8a–c}$$

The perturbation ageostrophic velocities u'_a and v'_a both scale with V_{ttw} because of their similarity in figure 5. These quantities are a combination of the buoyancy gradient (or v_g) and the vertical mixing strength induced by the wind stress.

A comparison can be made with an analogous scaling estimate for a field of mixed-layer eddies generated by the surface-layer baroclinic instability of a mean horizontal buoyancy gradient in Fox-Kemper, Ferrari & Hallberg (2008), Bachman & Taylor (2016), *viz.* $\Phi_{mle} \sim 0.1 h_0^2 \partial_x \overline{b}/f = 0.1 h_0 \overline{V}_g$, which is accompanied by a vertical restratification buoyancy flux estimate of $\overline{w'b'} \sim \Phi_{mle}\partial_x \overline{b} = 0.1 f \overline{V}_g^2$ (cf. BF_v/ℓ in (4.19)).

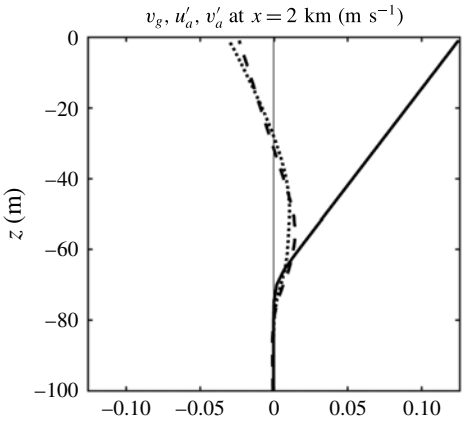

FIGURE 5. Vertical profiles of $\boldsymbol{u}$ in the centre of the northward jet at $x = 2$ km for a dense filament with $\theta_\tau = 0$ (as in figure 1*b*,*d*,*f*): $v_g(z)$ is the solid line, u'_a is dashed and v'_a is dotted. The TTW surface $\boldsymbol{u}'_a(0)$ is rotated cyclonically relative to $\boldsymbol{u}_g(0)$ by a little more than $3\pi/4$, reverses sign with depth and vanishes near $z = -h$.

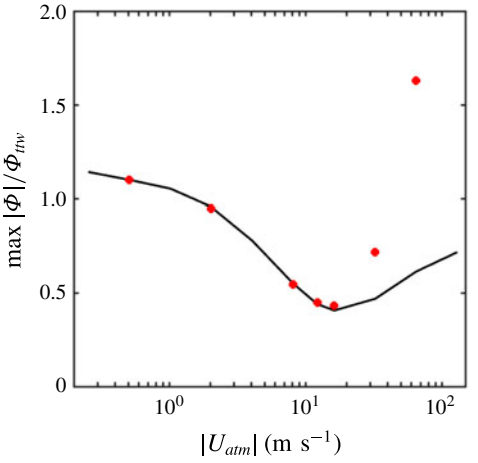

FIGURE 6. Ratio of the maximum absolute value of the linear TTW secondary-circulation streamfunction Φ for a dense filament to the scaling estimate Φ_{ttw} as a function of the wind speed U_{atm}. The filament axis is parallel to $\hat{\boldsymbol{y}}$. The black line is for cases with $\theta_\tau = 0$ (eastward wind), and the red points are for selected wind speed values for cases with $\theta_\tau = \pi/2$ (northward wind).

Notice by comparing figures 2 and 5 that the magnitudes of u'_a and u_∞ are similar. The ratio of their scaling estimates in (4.8) and (4.2) is

$$\frac{V_{ttw}}{V_{ek}} = 0.1\frac{V_g}{u_*}, \tag{4.9}$$

which is approximately one for the parameters in (3.7).

In figure 6 the aptness of this scaling estimate is demonstrated over nearly three decades in $|\boldsymbol{U}_{atm}|$. For low and intermediate winds, there is no directional dependence

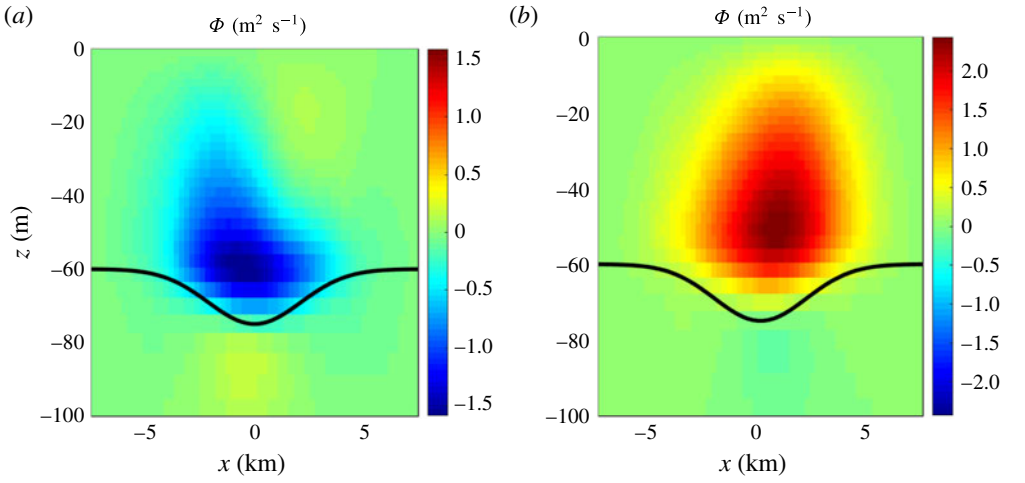

FIGURE 7. Linear TTW secondary-circulation streamfunction $\Phi(x, z)$ for a dense filament with $|\boldsymbol{U}_{atm}| = 32.8$ m s^{-1}: $\theta_\tau = 0$ (a) and $\theta_\tau = 0.5\pi$ (b). The $b(x, z)$, $h(x)$ and $v_g(x, z)$ fields are the same as in figure 1(*b*,*d*,*f*), and the $v_v(x, z)$ field has the same pattern but an amplitude proportional to the different u_* value (i.e. four times larger).

in Φ, as discussed above and as presumed in (4.6), while for high winds there is a directional dependence that is evident in both figures 6 and 7; nevertheless over this whole wind speed and direction range, Φ_{ttw} is an $O(1)$ accurate estimate for max[$|\Phi|$].

At large U_{atm}, the presence of v_g is less important in the secondary circulation within the central filament region than is the variation in $v_v \propto h(x)$ in the KPP parameterization (3.6); i.e. this regime is one with a spatially varying Ekman layer across the submesoscale flow structure. (The model here assumes that the filament structure in $b(x, z)$ survives the intense boundary-layer turbulence under a very high wind, which it might not do.) A scaling estimate is $u_a' \sim u_\infty(\delta h/h_0)$ because $\delta v_v/v_v = \delta h/h_0$ in (3.6). Using (3.3), (3.5), and (4.2), this implies

$$V_{\delta h} = \frac{u_*^2 V_g \ell}{N_0^2 h_0^3}, \quad W_{\delta h} = \frac{u_*^2 V_g}{N_0^2 h_0^2}, \quad \Phi_{\delta h} = \frac{u_*^2 V_g \ell}{N_0^2 h_0^2}. \tag{4.10a–c}$$

Because of the abundance of scaling estimates in this paper, in this and most of the further estimates below an $O(1)$ non-dimensional coefficient, fitted to the actual solutions, is left out for brevity; in any event its magnitude will depend on the submesoscale functional shapes, as noted for C_v and C_ζ after (3.5).

As u_* increases for fixed V_g, the ratio of this secondary-circulation streamfunction to the TTW one in (4.8) is

$$\frac{\Phi_{\delta h}}{\Phi_{ttw}} = \frac{V_{\delta h}}{V_{ttw}} = 10\frac{u_*}{f_0 \ell}\left(\frac{N_0 h_0}{f_0 \ell}\right)^{-2}, \tag{4.11}$$

i.e. the product of a Rossby number based on u_* and an inverse Burger number for the surface layer h and the interior stratification N_0. This reaches a value around one for $U_{atm} \approx 40$ m s^{-1}, consistent with the $O(1)$ directional difference in figure 7 at that U_{atm} value. The reason for the directional difference is that $u_a(z)$ is more surface trapped in an Ekman layer for $\theta_\tau = 0$, where the Ekman transport, $T_T^y < 0$, is along the filament,

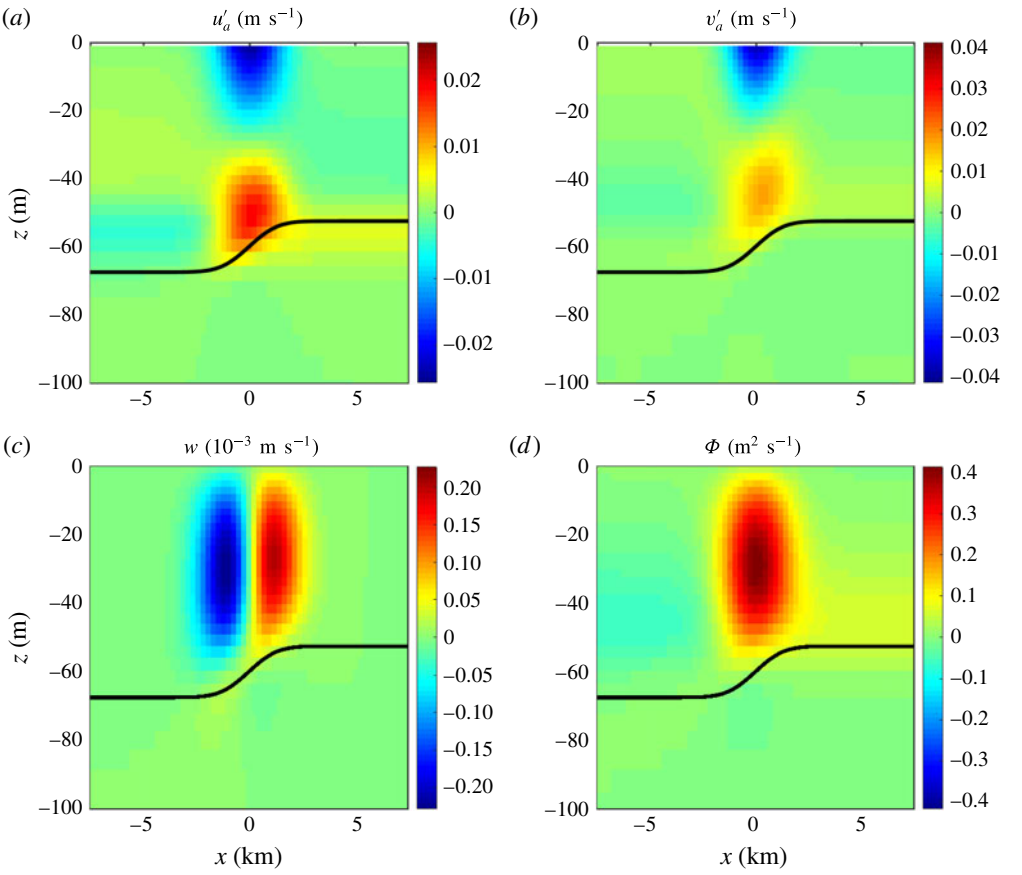

FIGURE 8. Linear TTW secondary circulation for a front with $\theta_\tau = 0$: (*a*) $u'_a(x, z)$ and $v'_a(x, z)$ (*b*) after subtracting the far-field averaged $\overline{\boldsymbol{u}}(z)$, and $w(x, z)$ (*c*) and $\Phi(x, z)$ (*d*). Note that the far-field values are small but non-zero because of the modestly different Ekman profiles $\boldsymbol{u}_\infty(z)$ on the two sides. The accompanying b, v_g, ν_v fields are in figure 1(*a*,*c*,*e*).

than it is for the case of $\theta_\tau = \pi/2$, where $T^x_T > 0$ is across the filament. The difference of two analytic Ekman-layer solutions with different constant ν_v values (i.e. a larger one in the filament centre), shows an analogous sign reversal and magnitude difference in the associated $\Delta\Phi(z)$ between the two θ_τ values in figure 7.

For a front the linear TTW solution is very similar to that from a dense filament except for the change of shape for $b(x, z)$ and $(\nu_v, \kappa_v)(x, z)$ (figure 1*a*,*c*,*e*). The far-field velocity profile is now different on both sides because h is different: the two far-field $\boldsymbol{u}(z)$ shapes are similar to figure 2, but with the vertical scale compressed or expanded with the different far-field h values, and the associated $\boldsymbol{u}$ magnitude is increased or decreased accordingly to conform to the transport integral constraint (4.1). The secondary circulation is again confined to the vicinity of the front and to within the surface layer (figure 8). Its shape is now a single cell in Φ, with upwelling on the light side and surface flow toward the dense side. The $v'_a(x, z)$ again acts to reduce the geostrophic shear. The maximum value of $Ro_g = \zeta_g/f_0$ is 1.04, and again the vorticity is reduced by TTW to a value of $Ro = \zeta/f_0 = 0.70$. The peak value of Φ is reduced

by approximately 10 % for the front compared to the filament, but, because of shape differences in their $b(x, z)$, the peak downwelling value of w is reduced by about 30 % for the front.

For the parameters (3.7), the secondary circulation for a front is again independent of wind direction θ_τ. For large U_{atm} the vertical velocity is one-signed at the front, with a monotonic x variation across the front in $\Phi(x, z)$ from (4.4) (not shown). Again the sign and magnitude of w differ with θ_τ: w is larger and positive for a north wind when U_{atm} is large, compared to smaller and negative with an east wind. The scaling estimates (4.2), (4.8), and (4.10) remain valid for fronts as well.

4.3. *Frontogenetic tendency and buoyancy flux*

In the presence of the secondary circulations in the preceding section, there are implications for further evolution of the submesoscale structure expressed as frontogenetic tendencies in velocity and buoyancy (§ 2.2) and as vertical and horizontal buoyancy fluxes (3.8) across the structure.

For the velocity gradient the frontogenetic tendencies are shown in figure 9. The sum of the advective and pressure force tendencies, $\mathcal{T}^{\boldsymbol{u}}_{adv\,\phi} = \mathcal{T}^{\boldsymbol{u}}_{adv} + \mathcal{T}^{\boldsymbol{u}}_{\phi}$, is clearly positive in the upper centre of the filament, as well as on both sides of the front, especially on the dense side. These are partly balanced by negative tendencies associated with the vertical mixing, $\mathcal{T}^{\boldsymbol{u}}_{\nu_v}$. The sum of these, $\mathcal{T}^{\boldsymbol{u}}$, is also positive in the upper centre of the dense filament and the upper dense side of the front, but negative on the upper light side. Thus, there is an important positive frontogenetic tendency near the surface for both types of submesoscale flow structure, with a net frontolytic tendency on the upper light side of the front. (It is known from time integration that in fact the TTW secondary circulation drives a dense filament toward a frontogenetic singularity in ζ and $\partial_x u$ (McWilliams *et al.* 2015).) The maxima of $\mathcal{T}^{\boldsymbol{u}}$ are 0.8 and 1.8×10^{-13} s^{-3} for the front and filament, respectively. In all the contributing tendencies for $\mathcal{T}^{\boldsymbol{u}}$, the magnitudes are about 50 % smaller for the front compared to the filament.

The patterns in figure 9 can be understood by identifying the dominant contributions to $\mathcal{T}^{\boldsymbol{u}}$. They are associated with the horizontal strain component $\partial_x u$ and the along-axis velocity v that is primarily geostrophic v_g; i.e.

$$\left.\begin{array}{c} \mathcal{T}^{\boldsymbol{u}}_{adv\,\phi} \approx -\partial_x u(\partial_x v_g)^2 - f_0 \partial_x u \partial_x v_g, \\ \mathcal{T}^{\boldsymbol{u}}_{\nu_v} \approx \partial_x v_g \partial_x \partial_z (\nu_v \partial_z v_g). \end{array}\right\} \tag{4.12}$$

Because f_0 and $\zeta_g = \partial_x v_g$ are of the same order in these solutions, both terms in $\mathcal{T}^{\boldsymbol{u}}_{adv}$ here contribute comparably. The relevant patterns of u'_a and v_g for the dense filament and front are evident in figures 1, 4 and 8.

This leads to a scaling estimate for $\mathcal{T}^{\boldsymbol{u}}_{adv}$ based on the first right-hand side term in (4.12) and Φ_{ttw} in (4.8), *viz.*

$$\mathcal{T}^{\boldsymbol{u}}_{adv\,ttw} = 0.1 \frac{u_* V_g^3}{f_0 h_0 \ell^3}. \tag{4.13}$$

With the parameter values in (3.7), this estimate is within an $O(1)$ value of the solutions for both the front and filament. It is evidently a highly nonlinear quantity, so the actual results have numerical values that are sensitive to the specific shape choices, though the patterns are robust. For solutions with smaller Ro_g values, the

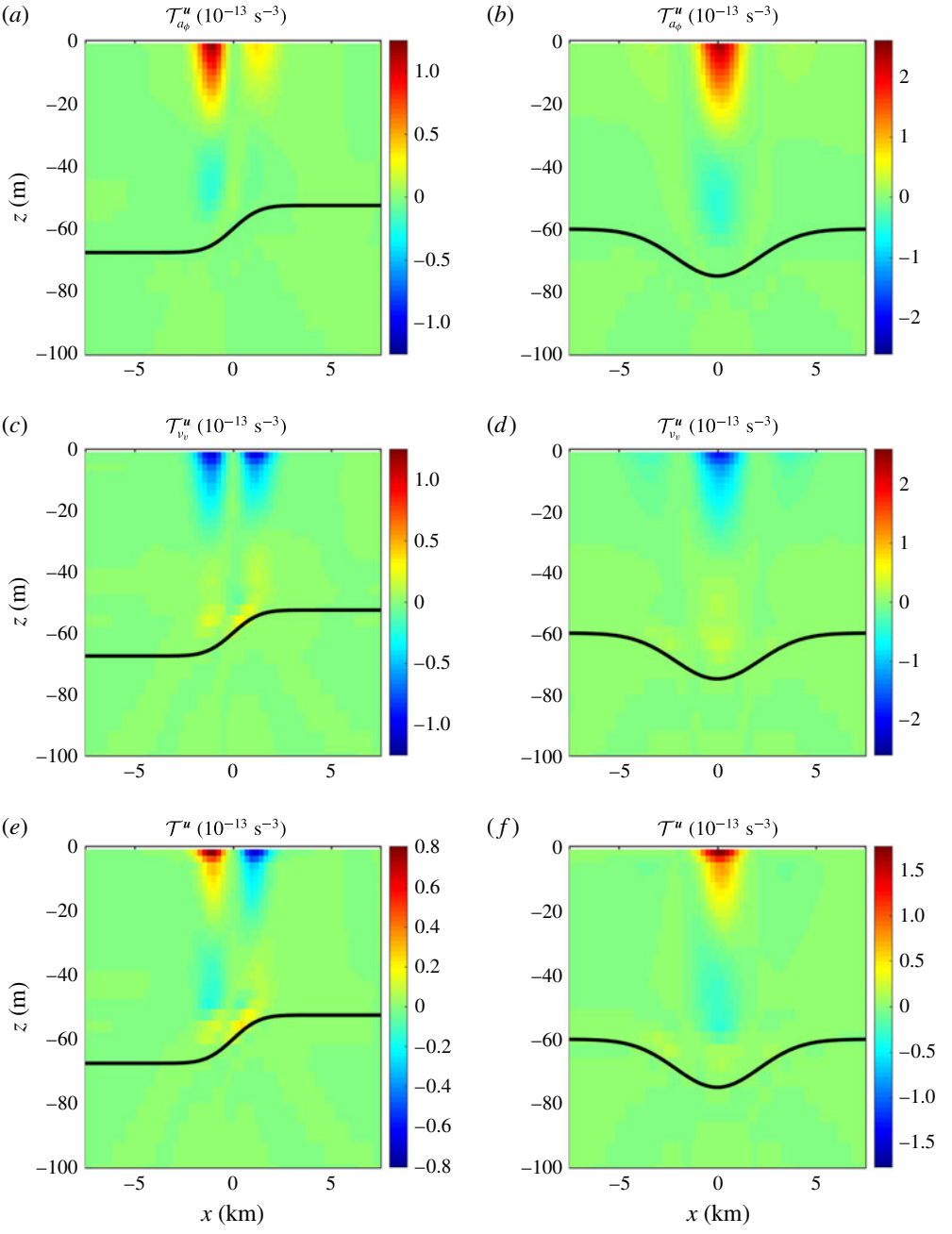

FIGURE 9. Frontogenetic velocity-gradient tendencies from (2.23). The sum of $\mathcal{T}^{u}_{adv\,\phi} = \mathcal{T}^{u}_{\phi} + \mathcal{T}^{u}_{adv}$ is in (*a*,*b*), $\mathcal{T}^{u}_{v_v}$ is in (*c*,*d*) and the total $\mathcal{T}^{u}$ is in (*e*,*f*). The front and dense filament solutions are in (*a*,*c*,*e*) and (*b*,*d*,*f*), respectively. These are for the standard parameters (3.7) with $\theta_\tau = 0$.

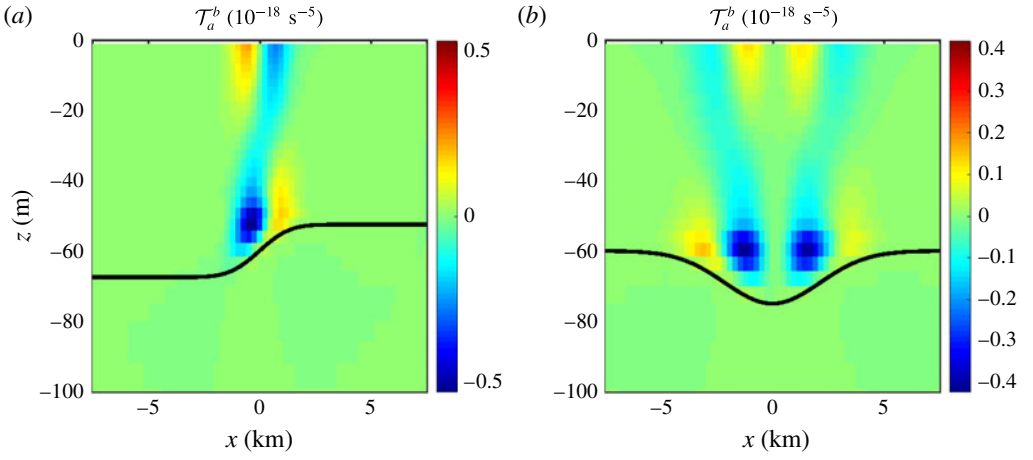

FIGURE 10. Advective frontogenetic buoyancy-gradient tendency $\mathcal{T}^b_{adv}$ from (2.22) for the front (*a*) and dense filament (*b*). Because $\mathcal{T}^b_{\kappa_v}$ is small, these are approximately the total tendency $\mathcal{T}^b$. These TTW solutions are for the standard parameters (3.7) with $\theta_\tau = 0$.

estimate should be based on the second right-hand side term in (4.12) that will be the larger one; i.e.

$$\mathcal{T}^{\boldsymbol{u}}_{\phi\, ttw} = 0.1\frac{u_* V_g^2}{h_0 \ell^2}, \tag{4.14}$$

whose ratio to (4.13) is Ro_g^{-1}. With the same scaling for ν_v following (4.6),$\mathcal{T}^{\boldsymbol{u}}_{\nu_v}$ has the same scaling as $\mathcal{T}^{\boldsymbol{u}}_{\phi}$. Thus, it is a parametrically robust result that the total $\mathcal{T}^{\boldsymbol{u}}$ has a frontogenetic shape similar to figure 9, bottom, because of the similar scaling among its component tendencies when $Ro_g \sim 1$.

A similar evaluation is made for the buoyancy-gradient advective tendency $\mathcal{T}^b_{adv}$ in figure 10. For these solutions the diffusive tendency is negligible because $\partial_z b$ is small where κ_v is not small. The dominant contribution is again associated with the horizontal strain,

$$\mathcal{T}^b_{adv} \approx -\partial_x u (\partial_x b)^2. \tag{4.15}$$

Thus, the patterns of u'_a and b' explain the four-centred structure for the front, with moderate frontogenesis in the upper dense side where there is surface horizontal convergence and somewhat stronger frontolysis in the lower dense side where there is divergence in the lower part of the boundary layer. For the dense filament, this pattern is simply doubled, as expected from the remark that a filament is a kind of double front in u'_a and b. (This perspective is not as useful for $\mathcal{T}^{\boldsymbol{u}}$, where the central cyclonic shear in a dense filament is the single dominant influence compared to the peripheral shears.) By the same rationale as for (4.13), the scaling estimate here is

$$\mathcal{T}^b_{adv\, ttw} = 0.1\frac{f_0 u_* V_g^3}{h_0^3 \ell}, \tag{4.16}$$

and it is quantitatively apt for the solutions here.

If $\mathcal{T}^{\boldsymbol{u}}_{adv\, ttw}$ and $\mathcal{T}^b_{adv\, ttw}$ are normalized by the velocity- and buoyancy-gradient variances, respectively, a frontogenetic rate is estimated as

$$r_{ttw} = 0.1\frac{u_*}{h_0} Ro_g, \tag{4.17}$$

which is the same for both frontogenetic tendencies. The same normalization for $\mathcal{T}^{\boldsymbol{u}}_{\phi\, ttw}$ yields an estimate of

$$r_{ttw\,\phi} = 0.1\frac{u_*}{h_0}. \tag{4.18}$$

This latter estimate can be interpreted as the inverse of a multiple of the turbulent eddy-turnover time in a wind-driven boundary layer, where the turbulent kinetic energy scales as u_*^2. Notice that r does not depend on the submesoscale structural parameters V_g and ℓ except through Ro_g.

Another comparison for r_{ttw} is with the geostrophic t_{eddy}^{-1} discussed in § 1. Their scaling ratio is $0.1\ u_*/(f_0 h_0)$, which for present parameters has a value of approximately 0.2. Thus, even in coherent structures like 2-D fronts and filaments, with no conservative evolutionary tendencies (i.e. t_{cs}^{-1} is zero), the ageostrophic advective frontogenetic rate associated with the TTW circulation is not that much smaller than the turbulent eddy-turnover time for geostrophic advection in an incoherently configured eddy field.

As with the secondary circulation (§ 4.2), there is little dependence of $\mathcal{T}^{\boldsymbol{u}}$ and $\mathcal{T}^{b}$ on the wind direction θ_τ as long as Φ_{ttw} in (4.8) is not small compared to $\Phi_{\delta h}$ in (4.10).

The buoyancy fluxes for both the front and filament are plotted in figure 11. The vertical flux BF_v is everywhere positive and peaks in the middle of the surface layer. This is a restratification flux and represents a conversion from available potential energy to kinetic energy. Its vertical shape is controlled mainly by $w(z)$ because b' varies little with z in the surface layer. It is somewhat larger for the filament than the front, consistent with its larger w. Because it is controlled by the secondary circulation (i.e. by w), it also does not depend on θ_τ for the standard parameters (3.7). A scaling estimate based on Φ_{ttw} is

$$BF_{v\ ttw} = 0.1\frac{u_* V_g^2 \ell}{h_0}, \tag{4.19}$$

whose magnitude is close to the peak value in figure 11(*b*,*d*), and whose approximate vertical buoyancy flux per unit area is $\overline{w'b'} = BF_{v\ ttw}/\ell$. This restratification flux can be interpreted by comparison with an equivalent surface heat flux per unit area, $Q = (\rho_0 c_p/\alpha^* g)\max_z[BF_v(z)]/\ell \approx 200$ W m^{-2} (where $c_p \approx 4\times 10^3$ m^2 s^{-2} K^{-1} is the heat capacity of seawater and $\alpha^* \approx 2\times 10^{-4}$ K^{-1} is the thermal expansion coefficient); i.e. BF_v is not small.

For BF_h, however, there is an important dependency on wind direction, as demonstrated by the much larger values for $\theta_\tau = \pi/2$ than for $\theta_\tau = 0$. The reason is the influence of $u_\infty(z)$. For all wind directions, $u_a'(z)$ reverses with depth (figure 4*a*) and so has partly cancelling contributions to the integrand in BF_h. The same is true for $u_\infty(z)$ for an eastward wind whose T_T^x in (4.1) is zero. However, for a northward wind, $u_\infty(z)$ is mostly eastward at all depths and $T_T^x = u_*^2/f_0 > 0$, so the horizontal buoyancy flux is much larger. A scaling estimate for the TTW secondary-circulation buoyancy flux is

$$BF_{h\ ttw} = 0.1\frac{u_* V_g^2 \ell}{h_0}, \tag{4.20}$$

which is the same as in (4.19). An estimate for the horizontal Ekman buoyancy flux, when $\boldsymbol{T}_T$ in (4.1) is directed across the front or filament, is

$$BF_{h\ ek} = \frac{u_*^2 V_g \ell}{h_0}. \tag{4.21}$$

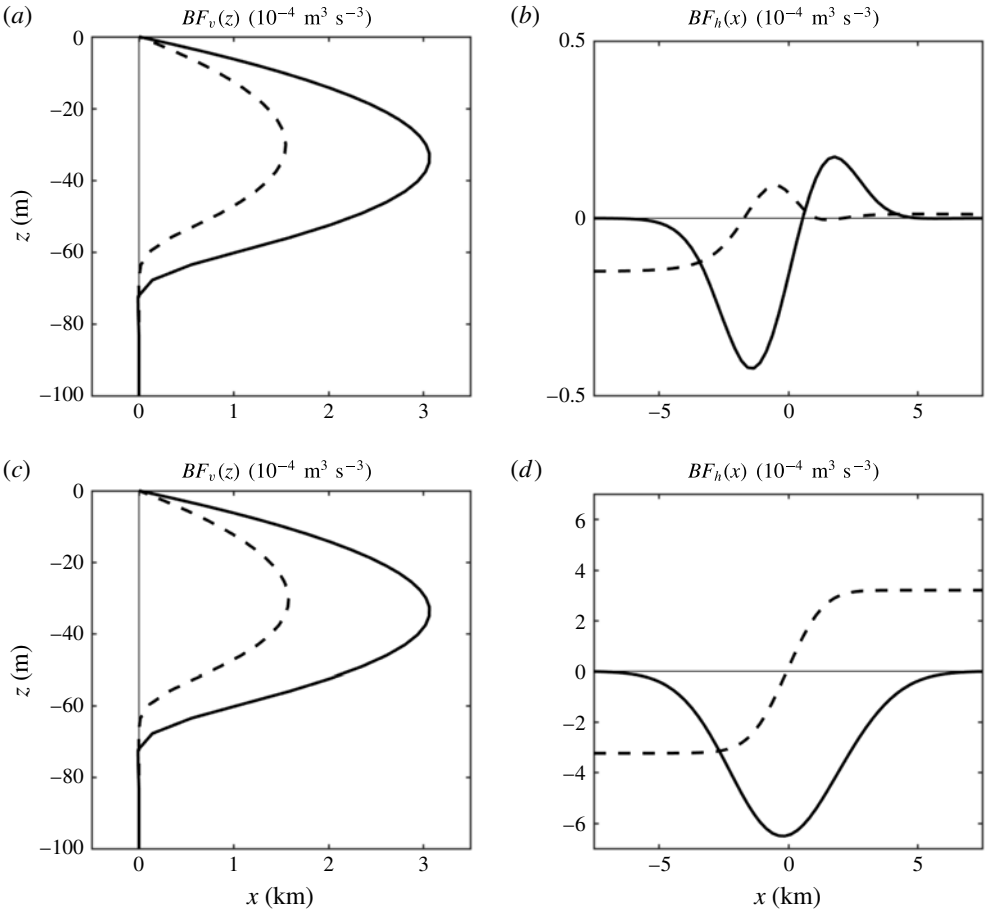

FIGURE 11. Integrated buoyancy fluxes (3.8) for the front (dashed lines) and dense filament (solid lines) with the parameters in (3.7). Panels (*a*,*c*) and (*b*,*d*) are $BF_v(z)$ and $BF_h(x)$, respectively. Panels (*a*,*b*) and (*c*,*d*) are for $\theta_\tau = 0$ and $\pi/2$, respectively. Note the change of scale for BF_h between the two wind directions.

Their ratio is formally the same as (4.9), i.e. ≈ 1 for the parameters in (3.7), but the actual solutions in figure 11 indicate that the estimator $BF_{h\ ttw}$ is too large by approximately a factor of 20 because of the sign reversal in u'_a with depth, which causes opposing fluxes across the buoyancy gradient.

The shape of BF_h is controlled by the shape of $u(x, z)$ times the surface $b'(x, 0)$, which is approximately the shape of $b'(x, z)$ throughout the surface layer. For the secondary circulation component u'_a, the sense of the horizontal flux is from higher buoyancy toward lower. For the dense filament this implies a horizontal buoyancy convergence toward the centre, while for the front it is a flux across the front toward the dense side. For the Ekman component, because $u_\infty(z)$ is independent of x, $BF_h(x)$ has the shape of $b'(x, 0)$, and thus is across the buoyancy gradient; in fact, replacing u by u_∞ in the BF_h integrand in (3.8), so that $BF_h(x) \propto b'(x, 0)$, is quite an accurate approximation for $\theta_\tau = \pi/2$. The simplest evolutionary interpretation in this case is that the Ekman buoyancy flux implies a bulk horizontal movement of the submesoscale b' structure in the direction of T^x_T, which would therefore have no

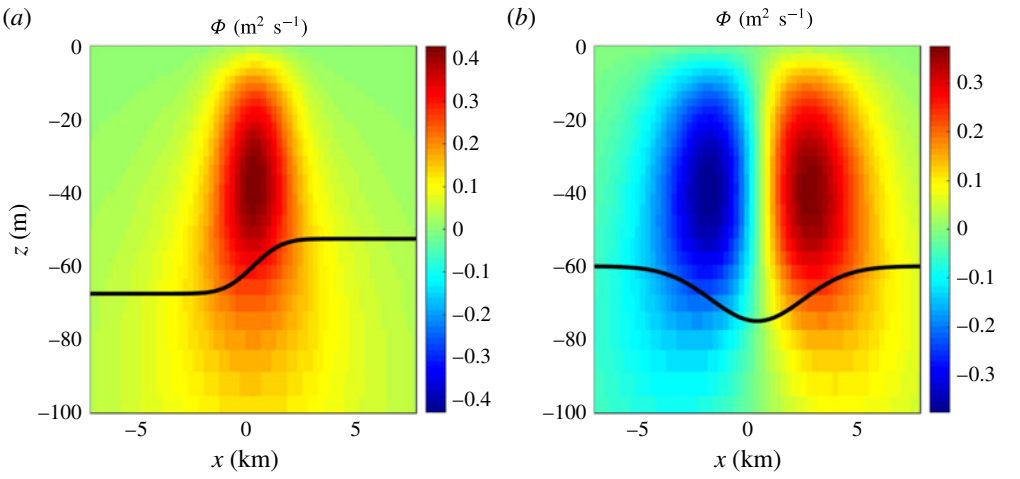

FIGURE 12. Linear strain-induced, secondary-circulation streamfunction $\Phi(x, z)$ for a front (*a*) and dense filament (*b*). These cases have $\alpha = 10^{-5}$ s^{-1} but no wind stress or vertical mixing. These can be compared to the topologically similar TTW Φ patterns in figure 8(*b*,*d*), and figure 4(*d*), respectively.

reflection in w, $\mathcal{T}^{\boldsymbol{u}}$ or $\mathcal{T}^{b}$, all of which are nearly independent of θ_τ. Alternatively, there may be vertically differential advection of $b'(x, z)$ by (u, w), which would be expressed in other evolutionary changes in the structure's shape than those evident in the *BF* profiles. In some circumstances with down-front wind stress, especially with weak interior stratification N_0, the horizontal buoyancy flux can advect dense fluid over lighter fluid and induce gravitational instability; furthermore, down-front winds can deplete the potential vorticity of the surface layer and induce centrifugal (symmetric) instability (Thomas 2005; Taylor & Ferrari 2009).

As the wind direction varies away from $\theta_\tau = 0$, there will be a transition from $BF_{h\ ttw}$, which is essentially independent of θ_τ, to $BF_{h\ ek}$ with a weighting factor of $\sin[\theta_\tau]$.

5. Linear strain solutions

Because the historical focus on fronts and frontogenesis has largely been on strain-induced secondary circulations (Hoskins 1982), in this section such solutions are presented for comparison with the TTW solutions in § 4. The neglect of $\mathcal{N}$ is continued, pro tem.

If $\boldsymbol{\tau} = \nu_v = \kappa_v = 0$ and $\alpha \neq 0$, then the TTW subsystem (2.15) has a simple solution:

$$u_T = -\left(\frac{\alpha}{f_0}\right)\frac{v_g + v_O - (\alpha/f_0)u_O}{1-(\alpha/f_0)^2}, \qquad v_T = \frac{v_g - (\alpha/f_0)u_O + (\alpha/f_0)^2 v_O}{1-(\alpha/f_0)^2}. \tag{5.1a,b}$$

If α is associated with the exterior strain field in mesoscale eddies, then typically $\alpha \ll f_0$. The solutions shown below have $\alpha = 10^{-5}$ s^{-1}, which is a value that gives similar SCFT magnitudes compared to the TTW solutions in § 4.

The strain-induced SCFT solutions have no far-field velocity, $\boldsymbol{u}_\infty = 0$, and no angle dependence (apart from the angle of the confluent deformation flow axis relative to the submesoscale frontal axis, here taken to be zero by the choice of $\boldsymbol{u}_d$ in (2.1)). For the $b(x, z)$ fields defined by (3.1) and (3.7), the secondary circulation streamfunction Φ in (4.4) has the patterns shown in figure 12. They are remarkably similar to the front and

dense filaments TTW Φ patterns in figure 8(*b*,*d*), and figure 4(*d*), respectively, *viz.* a single clockwise cell for a front and a pair of counter-rotating cells for a filament. By the choice of α here, even their magnitudes are similar. They do reach somewhat deeper into the stratified interior here. This is because they are not constrained by the boundary-layer confinement of ν_v and κ_v. Rather they have a penetration depth below the weakly stratified surface layer that is controlled by the interplay between the two left-hand side terms in the elliptic operator for the ΩE subsystem (2.20). This gives the so-called Prandtl depth of penetration, $h_p = f_0\ell/N_0$, which for present parameters is about 40 m, consistent with figure 12. Thus, because of their small ℓ, submesoscale surface-layer fronts do not induce vertical velocities deeply into the pycnocline when N_0 is large. In these α solutions, w_O is generally larger than w_T (obtained by applying the continuity equation to (5.1)) because of the α forcing term (2.21) in ΩE and the linear or higher power α/f_0 factors in (5.1).

Analogous to Φ_{ttw} and the associated secondary-circulation velocities in (4.8), an estimate for Φ_α comes from balancing the right-hand side α term in ΩE against the first left-hand side term (the second one is small in the surface layer), *viz.*

$$\Phi_\alpha = \frac{\alpha V_g h_0}{f_0}, \quad V_\alpha = \frac{\alpha V_g}{f_0}, \quad W_\alpha = \frac{\alpha V_g h_0}{f_0 \ell}. \tag{5.2a–c}$$

The ratio between the two influences on Φ is $10\alpha h_0/u_*$. Both estimates are linear in the factor V_g/f_0. Compared to the TTW secondary-circulation estimate in (4.8) and ignoring non-dimensional coefficients, α/f_0 plays the role here that u_*/f_0h_0 or $\nu_v/f_0h_0^2$ (a turbulent Ekman number) plays there. This comparison between secondary-circulation rates, $\alpha h_0^2/\nu_v$, was previously identified in Nagai *et al.* (2006), where it was argued that vertical mixing intensifies the secondary circulation around the Azores front.

For the strain-induced ageostrophic flow, v_a' is substantially smaller than u_a' for $\alpha/f_0 \ll 1$, in contrast to the TTW solution where the two components are more nearly equal. In partial explanation, equation (5.1) indicates that $u_T \sim (\alpha/f_0)v_g$ and $v_T \sim (\alpha/f_0)^2 v_g$, and the scaling estimate in (5.2) implies $u_a' \sim (\alpha/f_0)v_g$.

The frontogenetic tendencies $\mathcal{T}^{\boldsymbol{u}}$ and $\mathcal{T}^b$ are mostly positive for both fronts and dense filaments (figure 13). Only the total tendencies are shown, which in both cases is the sum of an advective tendency (i.e. $\mathcal{T}^{\boldsymbol{u}}_{adv\ \phi}$ in (2.23) and $\mathcal{T}^b_{adv}$ in (2.22)) and one proportional to α (i.e. $\mathcal{T}^{\boldsymbol{u}}_\alpha$ and $\mathcal{T}^b_\alpha$). The imprints of the α terms are clearly identified from their simple functional dependencies on $(\partial_x u)^2$ and $(\partial_x b)^2$, respectively. However, the magnitudes of the advective tendencies are similar and so make an appreciable contribution as well. The velocity gradient is frontogenetically intensified on the dense side of the front and in the centre of the filament, while the buoyancy gradient increases in the centre of the front and on the edges of the filament. Both qualitatively, and even quantitatively, these effects are similar to the TTW frontogenetic tendencies in figures 9(*e*,*f*), and 10, although there are some pattern differences as well, notably a deeper vertical extent for strain and a clearer indication of buoyancy frontogenesis. This similarity is to be expected from the similarity of the secondary circulations.

Frontogenetic tendency scaling estimates based on (5.2) are

$$\mathcal{T}^{\boldsymbol{u}}_\alpha = \frac{\alpha^3 V_g^2}{f_0^2 \ell^2}, \quad \mathcal{T}^b_\alpha = \frac{\alpha f_0^2 V_g^2}{h_0^2}. \tag{5.3a,b}$$

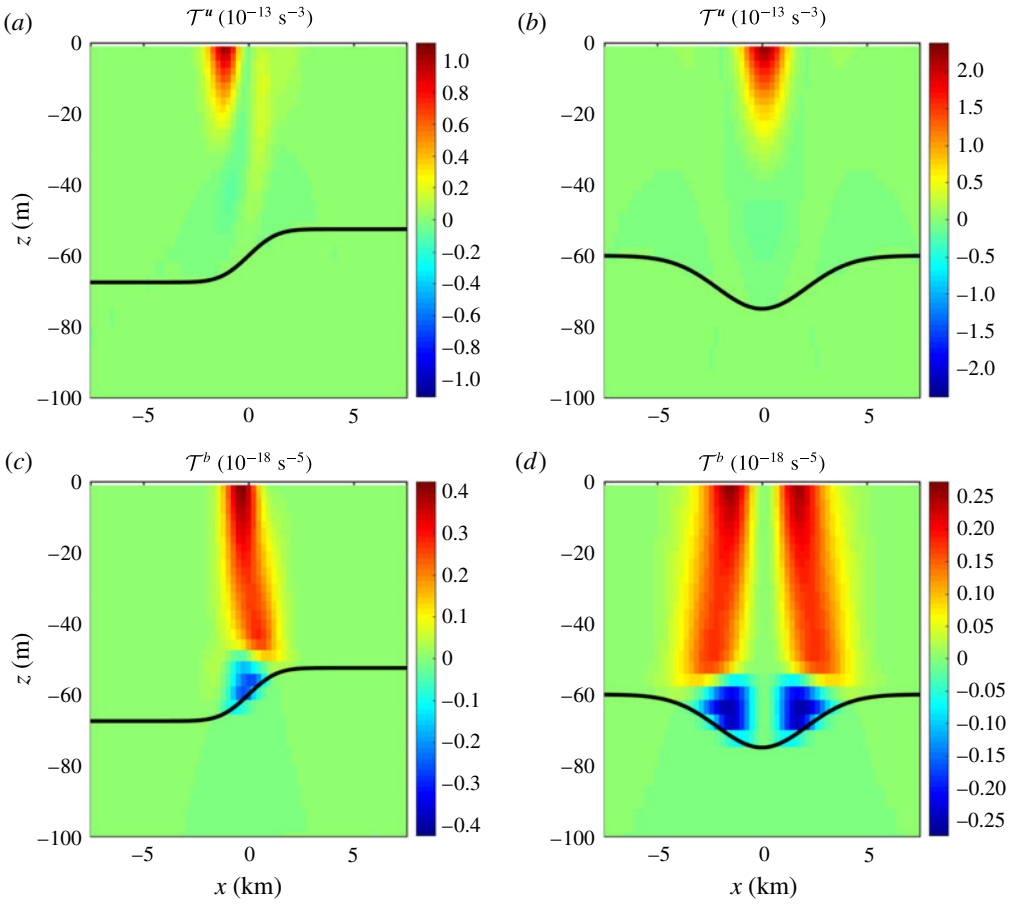

FIGURE 13. Frontogenetic velocity-gradient tendencies from (2.23) (*a*,*b*) and buoyancy-gradient tendencies from (2.22) (*c*,*d*). These are total tendencies due to advection and α. The frontal and dense filament solutions are in (*a*,*c*) and (*b*,*d*) respectively. These cases have $\alpha = 10^{-5}$ s^{-1} but no wind stress or vertical mixing. They can be compared to the rather different TTW $\mathcal{T}^{\boldsymbol{u}}$ in figure 9(*c*,*d*), and $\mathcal{T}^{b}$ in figure 10, even though the secondary-circulation advective tendencies, $\mathcal{T}^{\boldsymbol{u}}_{adv\,\phi}$ and $\mathcal{T}^{b}_{adv}$, are similar.

In the same way as § 4.3, equation (5.2) can be used to make estimates of the advective and pressure frontogenetic tendencies associated with the strain-induced secondary circulation:

$$\mathcal{T}^{\boldsymbol{u}}_{adv\,\alpha} = \frac{\alpha V_g^3}{f_0 \ell^3}, \quad \mathcal{T}^{\boldsymbol{u}}_{\phi\alpha} = \frac{\alpha V_g^2}{\ell^2}, \quad \mathcal{T}^{b}_{adv\,\alpha} = \frac{\alpha f V_g^3}{h_0^2 \ell}, \tag{5.4a–c}$$

where the subscript appendage α indicates the association with Φ_α. The total frontogenetic tendencies will be due to a combination of these different contributions.

The ratio of $\mathcal{T}^{\boldsymbol{u}}_{\alpha}$ to $\mathcal{T}^{\boldsymbol{u}}_{\phi\alpha}$ is $(\alpha/f_0)^2$, which is typically small, and its ratio to $\mathcal{T}^{\boldsymbol{u}}_{adv\,\alpha}$ is only a factor of Ro_g^{-1} larger. Therefore, the frontogenetic tendency for the velocity gradient is primarily due to the strain-induced secondary circulation rather than directly due to the straining rate directly. On the other hand, the ratio of $\mathcal{T}^{b}_{\alpha}$ to $\mathcal{T}^{b}_{adv\,\alpha}$ is

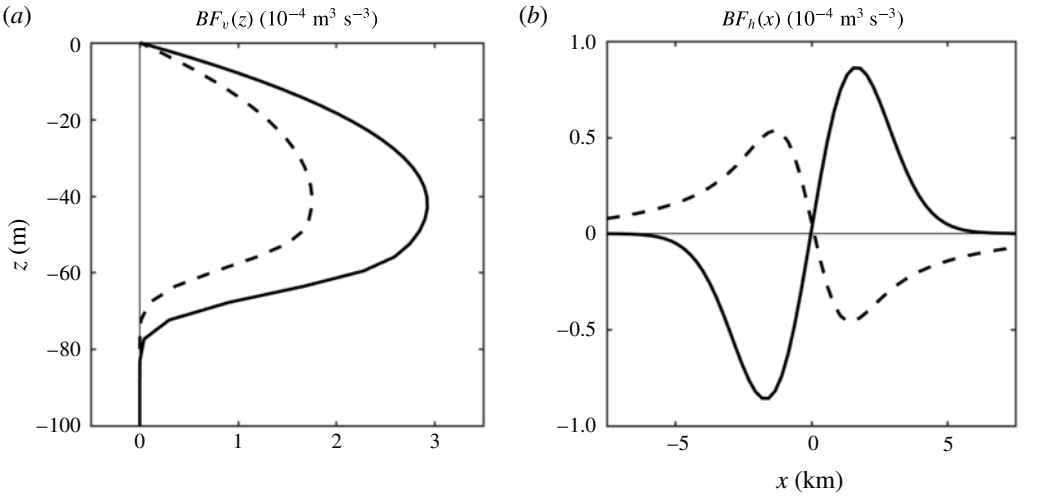

FIGURE 14. Integrated buoyancy fluxes (3.8) for the front (dashed lines) and dense filament (solid lines). Panels (*a*) and (*b*) are $BF_v(z)$ and $BF_h(x)$, respectively. These cases have $\alpha = 10^{-5}$ s^{-1} but no wind stress or vertical mixing. Here BF_v is quite similar to the TTW, profile in figure 11(*a*), but BF_h is only broadly similar to figure 11(*b*).

Ro_g^{-1}, which is ≈ 1 here. Thus, the direct straining effect is a primary influence on the buoyancy-gradient frontogenetic tendency, and the secondary circulation contributes comparably only when $Ro_g \sim 1$. This implies that strain-induced frontogenesis is especially effective, e.g. compared to TTW, in sharpening submesoscale buoyancy gradients.

These secondary-circulation frontogenetic tendencies can be compared with the TTW estimates in (4.13), (4.14), and (4.16), with the same ratio of $10\alpha h_0/u_*$ as seen from (5.2) for Φ_α/Φ_{ttw}.

When the dominant strain-induced velocity- and buoyancy-gradient frontogenetic tendencies in (5.3)–(5.4), *viz.* $\mathcal{T}^{\boldsymbol{u}}_{\phi\alpha}$ and $\mathcal{T}^{b}_{\alpha}$, are normalized by their respective gradient variances, the result is a frontogenetic rate estimate of

$$r^{\boldsymbol{u}}_{\alpha} = r^{b}_{\alpha} = \alpha, \tag{5.5}$$

i.e. the external deformation rate. (The normalized rate for $\mathcal{T}^{\boldsymbol{u}}_{adv\,\alpha}$ is $(\alpha/f_0)^2$ smaller.) This can be compared to r_{ttw} in (4.17) or (4.18); for the parameters in (3.7) and the value of $\alpha = 10^{-5}$ s^{-1} used here, $r_\alpha \approx r_{ttw}$.

The associated buoyancy flux profiles are in figure 14. The vertical flux $BF_v(z)$ is again a restratification flux (cf. figure 11*b*,*d*) with similar magnitudes to the TTW BF_v, and again the flux for the filament is stronger than the frontal flux. There are more differences among the $BF_h(x)$ profiles, mainly because of the absence of any Ekman $\boldsymbol{u}_\infty$ influence in the strain solution. The shapes are understandable as simple products of $u'(x, 0)$ and $b'(x, 0)$. For the front, u' is an x-symmetric negative flow from the light to the dense side near the surface, while b' is anti-symmetric with a positive anomaly on the light side. For the dense filament, u' is an anti-symmetric convergent flow, while b' is an even-symmetric negative anomaly. Scaling estimates based on Φ_α are

$$BF_{v\alpha} = BF_{h\alpha} = \alpha V_g^2 \ell, \tag{5.6}$$

and the ratio with their TTW counterparts in (4.19)–(4.20) is again $10\alpha h_0/u_*$. The $BF_{h\alpha}$ estimate is somewhat high because of the sign reversal with depth in $u_a'(z)$. This is consistent with BF_v values being somewhat larger than BF_h ones (excluding Ekman buoyancy flux for $\theta_\tau \neq 0$; § 4.3), in spite of having identical scaling estimates.

Thus, for a given frontal structure, the relative influences of TTW and strain on the SCFT behaviour vary in magnitude with u_*/h_0 and α, respectively. The solution behaviours are generally similar between the two influences. In combined solutions with $U_{atm} = 8.2$ m s^{-1} and $\alpha = 10^{-5}$ s^{-1} (not shown), the influences are generally reinforcing and close to a simple superposition in the SCFT outcomes.

Finally, to summarize the explanations for the secondary-circulation shape, consider the structural relations for the TTW and strain processes. For TTW, the horizontal shape of u_a' near the surface, denoted by $U_a(x)$, is opposite to $v_g(x, 0)$ (§ 4.2); i.e. $U_a(x) \sim -v_g \sim -\partial_x b(x, 0)$. (Dimensional scaling factors are ignored here.) Because of continuity the horizontal shape of $w \sim W(x)$ in the middle of the surface layer is $W(x) \sim \partial_x U_a(x) \sim -\partial_{xx} b(x, 0)$. For strain, by invoking the same principal balance in ΩE stated before (5.2) and assuming b' does not vary much with depth across the surface layer, $W(x) \sim -\partial_{xx} b(x, 0)$. These shape arguments are valid for both fronts and filaments. (In the filament case, the argument is for the strong central downwelling region, with $w > 0$ on the periphery for mass conservation.) Thus, the two $W(x)$ shapes are the same in TTW and strain-induced secondary circulations.

6. Nonlinear TTW solutions

The 2-D linear solutions of § 4 are generalized with $\mathcal{N} \neq 0$. In the TTW subsystem (2.15)–(2.16), the ratio of the ageostrophic horizontal advection in $\mathcal{N}_T^v$ to the Coriolis force is scale estimated as Ro_g, which is therefore an estimate of the importance of nonlinearity in SCFT solutions. In §§ 4–5, $\mathcal{N}^{\boldsymbol{u}}$ and $\mathcal{N}^b$ were neglected, even though $Ro_g \sim 1$ for the parameters in (3.7), but now this is remedied.

6.1. *Secondary circulation*

One effect of nonlinearity is to alter the Ekman transport relation (4.1), which generalizes to

$$\boldsymbol{T}_T = \int_{-\infty}^{0} \boldsymbol{u}_T(z')\,\mathrm{d}z' = \hat{\boldsymbol{z}} \times \left(\frac{\boldsymbol{\tau}}{f\rho_0} - \frac{1}{f_0} \int_{-h(x)}^{0} \mathcal{N}_T^{\boldsymbol{u}}\,\mathrm{d}z \right) \tag{6.1}$$

when $\mu_g = \alpha = 0$; i.e. for a 2-D front or filament, cross-axis momentum advection causes Ekman pumping at the base of the surface layer, with $w_{ek} \approx \partial_x T_T^x \neq 0$. On the other hand, as in § 5, the induced pycnocline circulation will only penetrate over the rather small depth scale of h_p for submesoscale flow structures. As in figure 3, $w_T \gg w_O$ in the surface layer, but with the advective contribution to (6.1), both components extend to the bottom of the domain, with $w_O = -w_T$ and $w = 0$ at depth.

Unlike the linear TTW solutions in § 4 (when $V_{\delta h} \ll V_{ttw}$ from (4.10)), advection causes a significant dependence on the wind direction θ_τ. The reason for this is that the dominant advection in the 2-D flows examined here is the cross-axis component, $u_a \partial_x \cdot$, and u_a has an important contribution from the far-field (Ekman) velocity, $u_{a\infty}(z)$ (e.g. figure 2). Figure 15 shows how the peak downwelling velocity varies with θ_τ for both fronts and dense filaments. The strongest w minima occur when u_a' constructively reinforces $u_{a\infty}$ in the upper part of the surface layer. In a dense filament with its approximate anti-symmetry with two signs of u_a' (figure 4*a*), this occurs for two wind

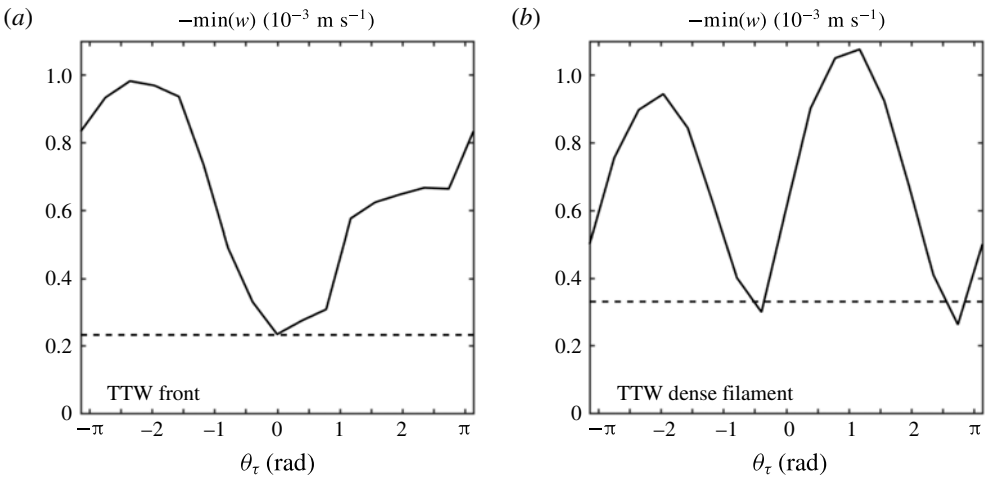

FIGURE 15. Spatial minima of $w(x, z)$ for nonlinear TTW solutions for a front (a) and a dense filament (b) with parameters (3.7) as a function of wind direction θ_τ. The dashed lines correspond to the minima in the linear TTW solutions in figures 4(c) and 8(c), respectively.

directions, approximately NE and SW, where the near-surface Ekman velocity is most nearly across axis. In a front with only a single sign for u'_a (figure 8a), the SW direction supports this constructive reinforcement. There is also a weak enhancement of $w < 0$ for a front with N to NE winds; in this case the upper-ocean TTW and Ekman u are opposing, but still there is a modest enhancement of $\partial_x u < 0$.

This rationalization of the θ_τ dependency is based on the nonlinear secondary circulation not being too different in its spatial patterns from the linear one. This is clearly so in the far field, where the linear and nonlinear solutions are exactly the same. It is only approximately so in the central region. It is clear from figure 15 (cf. the dashed lines) that the nonlinear circulation can be substantially stronger (by a factor up to 3-4 in w). The associated spatial patterns for the peak θ_τ values are shown in figures 16 and 17, and they are indeed generally similar in shape to their linear counterparts (i.e. figures 8c, and 4c, respectively). In particular, in all cases there is a downwelling w on the dense side of a front and near the centre of a dense filament. Besides the larger magnitudes for favourable θ_τ, the differences due to advection are mainly ones of sharper gradient, smaller width and greater x asymmetry.

For completeness, $T_T^w(x)$ from (6.1) is plotted for these nonlinear solutions in figure 18. It shows a tripole pattern for the front and a dipole pattern for the dense filament. The implied $w_{ek}(x)$ for the front is a tripole with a downwelling centre slightly west of the middle of the front, echoing the w pattern in figure 16 but different from the basic linear TTW dipole pattern in figure 8. For the filament, the implied w_{ek} is a dipole with downwelling west of the centre, as in figure 17 but again different from the basic linear TTW tripole in figure 1. Were h_p larger (i.e. with smaller N_0, bigger ℓ, or larger f_0), then these $w_{ek}(x)$ patterns would be more evident in the pycnocline, while they are rather faint in the present solutions. The strongest nonlinear $w(x, z)$ values occur in the surface layer, and they preserve the linear TTW shapes of a dipole for the front and an almost central downwelling for the filament. The secondary peak in $\min[w](\theta_\tau)$ for the dense filament with $\theta_\tau = -5\pi/8$

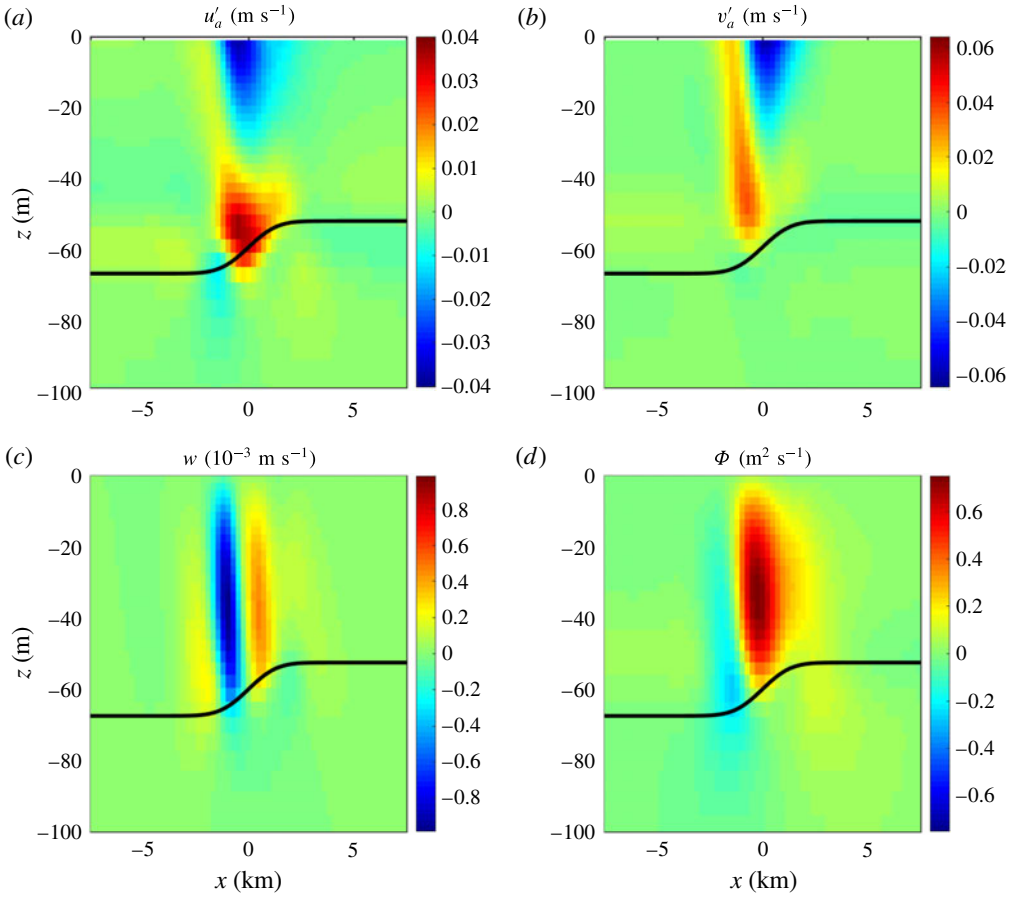

FIGURE 16. Nonlinear TTW secondary circulation for a front with $\theta_\tau = -3\pi/4$ and $Ro_g = 1.04$: (*a*,*b*) u'_a and v'_a after subtracting the far field $\boldsymbol{u}_\infty(z)$ in figure 2 and (*c*,*d*) w and Φ. This angle choice corresponds to the largest min[w] value in figure 15(*a*). The accompanying b, v_g, v_v fields are in figure 1(*a*,*c*,*e*), and the corresponding linear solution for the ageostrophic circulation is in figure 8.

has a $w(x, z)$ pattern with a similar narrow, downwelling branch as in figure 17 but mirror reflected to be displaced to the east of the filament centre.

A more formulaic way to understand the influence of nonlinearity is to focus on the y-momentum equation in (2.15) and estimate the incremental cross-axis velocity u_{TNL} by a balance with the Coriolis force; *viz.* with successive approximations,

$$f_0 u_{TNL} \approx -(u\partial_x v + w\partial_z v) \approx -u\partial_x v \approx -u_\infty \partial_x v_g. \tag{6.2}$$

These several approximations are rough ones (especially the last step with $u \approx u_\infty$), but they preserve much of the spatial structure and order of magnitude of the more general dynamical balances. This then is connected to the incremental effect on w by the continuity equation in the upper part of the surface layer,

$$\partial_x u_{TNL} = -\partial_z w_{TNL} \approx \frac{2}{h} w_{TNL}; \tag{6.3}$$

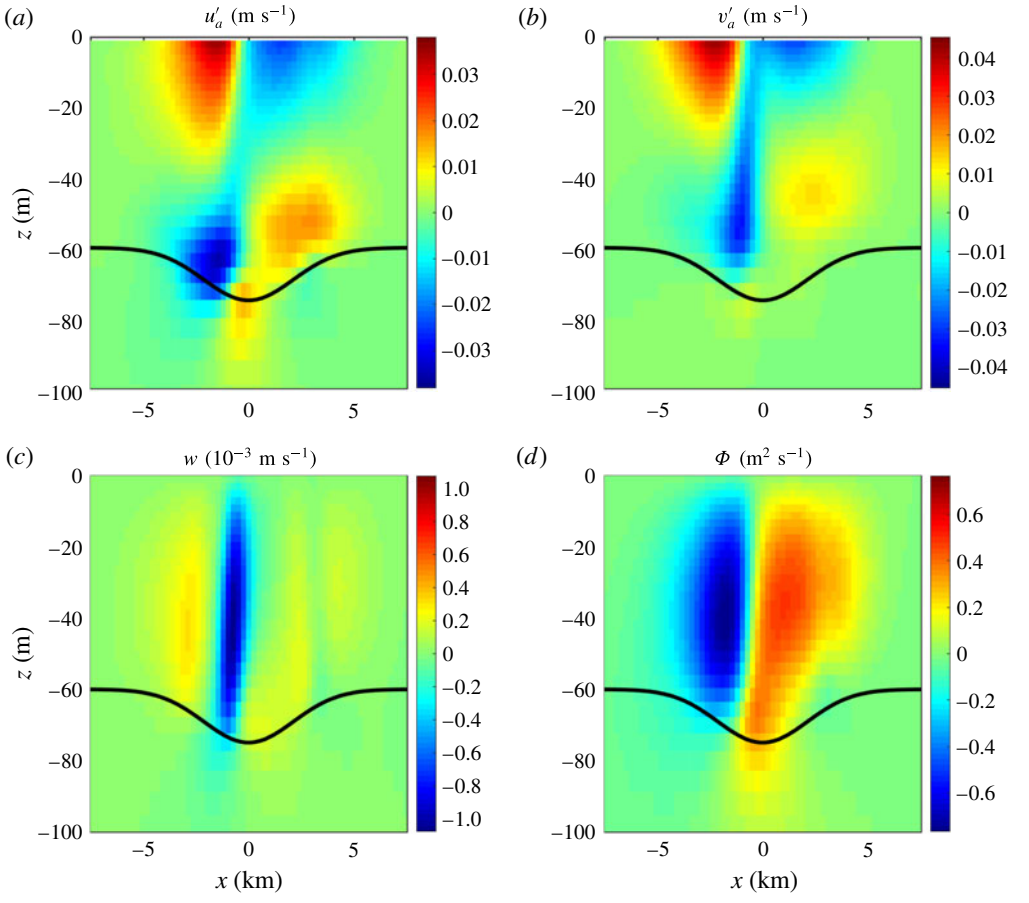

FIGURE 17. Nonlinear TTW secondary circulation for a dense filament with $\theta_\tau = 3\pi/8$ and $Ro_g = 1.32$: (*a*,*b*) u_a' and v_a' after subtracting the far field $\boldsymbol{u}_\infty(z)$ in figure 2 and (*c*,*d*) w and Φ. This angle choice corresponds to the largest min[w] value in figure 15(*b*). The accompanying b, v_g, v_v fields are in figure 1(*b*,*d*,*f*), and the corresponding linear solution for the ageostrophic circulation is in figure 4.

hence, the advectively generated vertical velocity in the centre of the surface layer is

$$w_{TNL} \approx -\frac{h}{2} u_\infty \partial_x \zeta_g. \tag{6.4}$$

From the simple shapes for the front (i.e. $u_\infty < 0$ with $\theta_\tau = -3\pi/4$, ζ_g a dipole with a positive lobe to the west, and $\partial_x \zeta_g$ with a central negative extremum) and the dense filament (i.e. $u_\infty > 0$ for $\theta_\tau = 3\pi/8$, ζ_g a positive monopole, and $\partial_x \zeta_g$ a central dipole with its negative lobe to the west side), the resulting shapes are thus explained for $w_{TNL}(x)$. It has a central downwelling for the front that adds to the dipole pattern for the linear TTW w to make an unequal dipole with strong downwelling in the west (cf. figure 16), and it has a dipole for the filament with its downwelling lobe to the west that adds to the central downwelling for linear TTW central w to make a dominant downwelling centre in the west (cf. figure 17).

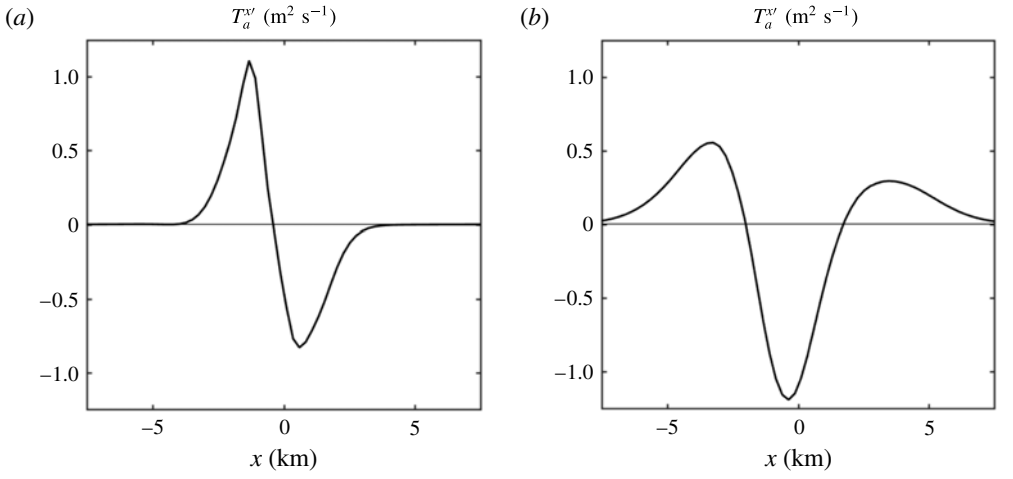

FIGURE 18. Ageostrophic transport anomaly $T_T^{xv}(x)$ from (6.1) across a front (a) and a dense filament (b) for $\theta_\tau = -3\pi/4$ and $3\pi/8$, respectively.

The same formulas as in (6.2) can be used to give a scaling estimate for the incremental secondary circulation due to nonlinearity. Here separate estimates for u are made based on either the Ekman velocity V_{ek} in (4.2) or the TTW circulation anomaly V_{ttw} in (4.8), whose inverse ratio is (4.9). The result is

$$\Phi_{NL} = \frac{u_* V_g}{f_0^2 \ell}\mathcal{F}, \quad V_{NL} = \frac{u_* V_g}{f_0^2 \ell h_0}\mathcal{F}, \quad W_{NL} = \frac{u_* V_g}{f_0^2 \ell^2}\mathcal{F}, \tag{6.5a–c}$$

where $\mathcal{F} = \max[0.1V_g, u_*]$. As expected their ratio with their linear counterparts in § 4 is Ro_g. For the solutions with parameters (3.7), the values of the arguments in $\mathcal{F}$ are approximately the same, which indicates that it is indeed the θ_τ values for constructive reinforcement between u_a' and u_∞ that generates the large w extrema in figures 16 and 17. Furthermore, although the previous argument emphasizes the role of $\mathcal{N}^v$, the contributions from $\mathcal{N}^u$ and $\mathcal{N}^b$ are also quantitatively important here where $Ro_g \sim 1$. For weaker submesoscale flows with $Ro_g \ll 1$, $\Phi_{NL} \propto u_*^2 V_g$, which is linear in V_g. As Ro_g further increases, $\Phi_{NL} \propto u_* V_g^2$; i.e. it becomes quadratic in V_g.

The other diagnostic quantities of interest also vary with θ_τ with curves at least broadly similar to the shape of $\min[w](\theta_\tau)$ in figure 15, but the magnitudes of their θ_τ dependencies differ; e.g. in figures 16 and 17, the nonlinear amplification of the extrema for $\boldsymbol{u}_a'$ and Φ is not as large as for w, by about 50 % and 75 %, respectively, rather than the 200 %–300 % for w. The amplification factors for each of the fields are similar between the front and filament. Furthermore, sharper horizontal gradients are evident in the nonlinear solutions.

As a function of Ro_g, the dependencies in (6.5) have begun to make their transition from the linear to the steeper quadratic variation with V_g by these $Ro_g \sim 1$ solutions. Furthermore, both of the extreme θ_τ cases shown here are close to the limit of iteration convergence for the TTW + ΩE system; i.e. very small values of γ in (2.24) and large iteration numbers are required, and convergence fails for further increases in δh_0 (i.e. in Ro_g). As discussed at the end of § 2.1, this is suggestive of a breakdown of balanced solutions. As Ro_g approaches the convergence limit, the diagnostic SCFT solutions do develop sharper spatial structures and rapidly

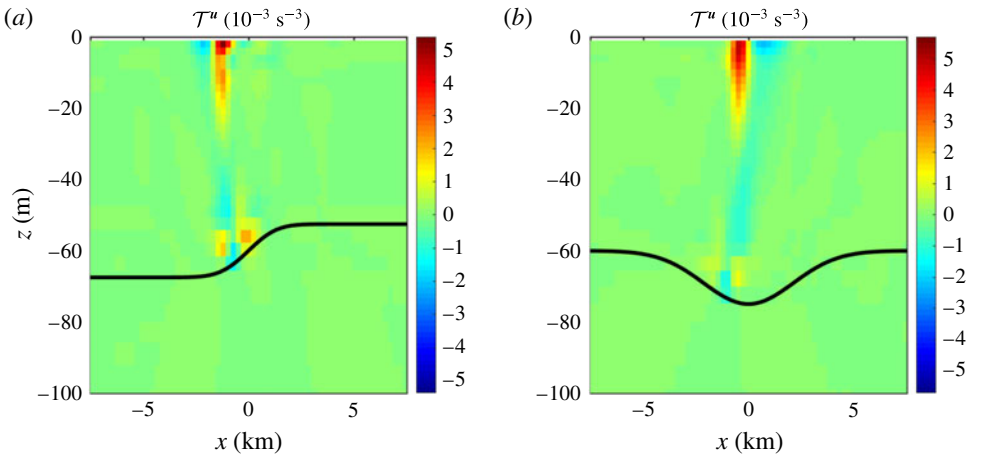

FIGURE 19. Frontogenetic velocity gradient tendencies $\mathcal{T}^u$ from (2.23) in nonlinear TTW solutions for a front with $\theta_\tau = -3\pi/4$ (a) and dense filament with $\theta_\tau = 3\pi/8$ (b). These angle choices correspond to the largest min[w] values in figure 15. They can be compared with their linear counterparts in figure 9(e,f).

increasing magnitudes, and, not surprisingly, a dependency develops on the discrete grid resolution (§ 3), which is not pursued here. The magnitude increases with Ro_g are possibly steeper than the quadratic dependency in the scaling estimate (6.5); the range of successful large Ro_g solutions is too small to determine this here. One can at least contemplate the possibility that balanced dynamics is approaching a finite-time singularity (n.b. Hoskins & Bretherton (1972) and McWilliams *et al.* (2015) for balanced strain-induced and TTW evolutionary frontogenesis, respectively).

6.2. *Frontogenetic tendency and buoyancy flux*

The frontogenetic velocity gradient tendencies $\mathcal{T}^u$ remain similar in pattern but amplified in magnitude and shrunk in scale due to nonlinearity for both the front and dense filament (figure 19). The peak positive values are on the west side of the centres. For a front, this is already the favoured location for $\mathcal{T}^u > 0$ in the linear TTW solution (figure 9e,f), and for both front and filament nonlinear TTW solutions it is also the location of peak surface convergence above the peak downwelling flow (figures 16 and 17). The nonlinear amplification factor for the peak values of $\mathcal{T}^u$ is similar to that for w. For these TTW solutions there is some but smaller nonlinear amplification in $\mathcal{T}^b$ (not shown).

The nonlinear TTW scaling estimate for $\mathcal{T}^u$ is amplified compared to the linear one (4.13) by the factor Ro_g, as it is for w in (6.5) as well. This implies a highly nonlinear dependency, $\mathcal{T}^u \propto (V_g/\ell)^4$. However, because of the substantial shape changes between linear and nonlinear w and $\mathcal{T}^u$, it is implausible that a simple magnitude scaling estimate like these will be very accurate when Ro_g is large.

The buoyancy flux profiles, $BF_v(z)$ and $BF_h(x)$ in (3.8), are relatively little affected by ageostrophic advection. The profile for $BF_v(z)$ always has a convex shape as in figure 11(b,d). Its peak amplitude increases somewhat with nonlinearity especially for θ_τ values close to the ones with the largest - min[w] values, but never by more than approximately 30 %. Thus, in spite of the large amplification in the peak value

of w, the horizontally integrated buoyancy flux is not greatly changed. The dominant influence on $BF_h(x)$ remains the Ekman transport dependency on θ_τ, with peak positive and negative fluxes for $\theta_\tau = \pm\pi/2$ where the cross-front transport is largest.

As with the linear solutions, in combined nonlinear TTW and α solutions, the SCFT behaviours are largely additive.

6.3. *Inaccuracy of the 'nonlinear Ekman-layer' model*

A widely used approximate model for the wind-driven surface boundary layer is the so-called nonlinear Ekman layer (NLE; Stern 1965). With the assumptions that (i) the horizontal scale of the wind stress is larger than that of the surface geostrophic current, (ii) the vertical scale of the geostrophic flow is larger than the depth of the boundary layer and (iii) the relevant Rossby numbers are small but finite, then the ageostrophic horizontal transport $\boldsymbol{T}_T$ and the vertical velocity at the base of the boundary layer, the Ekman pumping w_{ek}, are given by

$$\boldsymbol{T}(\boldsymbol{x}) = \hat{\boldsymbol{z}} \times \frac{\boldsymbol{\tau}}{\rho_0(f + \zeta_g(\boldsymbol{x}))} \quad \text{and} \quad w_{ek}(\boldsymbol{x}) = \hat{\boldsymbol{z}} \cdot \boldsymbol{\nabla} \times \frac{\boldsymbol{\tau}}{\rho_0(f + \zeta_g(\boldsymbol{x}))}, \tag{6.6a,b}$$

i.e. simple generalizations of the usual Ekman relations replacing f by $f + \zeta_g$ to include some advective nonlinearity. These formulas are convenient because they do not require solution of a differential equation in z, are independent of the vertical mixing profile $\nu_v(\boldsymbol{x}, z)$, and have a clear implication of a secondary circulation generated by wind over mesoscale currents and eddies. A partial motivation is the vector identity for horizontal momentum advection,

$$\zeta(\hat{\boldsymbol{z}} \times \boldsymbol{u}) + \tfrac{1}{2}\boldsymbol{\nabla}\boldsymbol{u}^2 = (\boldsymbol{u} \cdot \boldsymbol{\nabla})\boldsymbol{u}, \tag{6.7}$$

where at least part of the first left-hand side term (the vortex force) is retained in the NLE model. Niiler (1969) made a similar Ekman pumping analysis for the Gulf Stream with $v_g(x, y)$ by including an advective term in the y-momentum equation, $u_a \partial_x v_g$, but not its vortex force companion in the x-momentum equation; as explained in the rest of this section, this alternative avoids much of the criticism of Stern's proposal.

In the TTW + ΩE system, without explicitly invoking Stern's assumptions behind (6.6), the NLE approximation can be represented by replacing $\mathcal{N}_a^{\boldsymbol{u}}$ in (2.13) by

$$\mathcal{N}_{a\,NLE}^{\boldsymbol{u}} = -\zeta_g(\hat{\boldsymbol{z}} \times \boldsymbol{u}_a), \tag{6.8}$$

and otherwise neglecting ageostrophic advection. No assumption is made *a priori* that ζ_g is independent of z within the boundary layer but obviously such a situation is contained within (6.8). When SCFT solutions obtained with (6.8) are compared to the more complete solutions in the preceding part of this section, they are found to be consistently inaccurate in representing nonlinear advective effects even in the limit $Ro_g \to 0$.

There are several important deficiencies in (6.8), hence in (6.6). One has to do with the neglect of $\mathcal{N}^b$ in (2.13), but the NLE solution accuracy is not much better with or without including this term in ΩE. Another has to do with neglecting the suppressive effect of stratification, as expressed in w_O, but again this is not the primary cause of inaccuracy here (and will not be important when h_p is large enough). Rather it

is the false inclusion of the term $\mathcal{N}^u_{a\,NLE} = v_a\zeta_g$, which is absent in $\mathcal{N}^u_a$ and has a leading-order magnitude in a Ro_g expansion, larger than any of the other terms in $\mathcal{N}^u_a$. (In contrast, $\mathcal{N}^v_{a\,NLE} = -u_a\zeta_g$ is a correct leading-order term in the y-equation.) The fallacy is to keep this vortex force term in the x-momentum equation while neglecting its cancellation in the Bernoulli head, i.e. the second left-hand side term in (6.7). Thus, there often will be no convenient alternative for representing the effect of momentum advection in the boundary layer other than by solving a more complete system like the TTW + ΩE one used here.

7. Summary and discussion

Submesoscale density fronts and (dense) filaments in the upper ocean are long-lived coherent structures created by frontogenesis in association with ambient mesoscale buoyancy gradients and currents. Once they achieve a quasi-steady configuration (e.g. with along-axis symmetry), their further evolution, apart from possible instabilities, is primarily through ageostrophic advection by the secondary circulation generated by either ambient strain or turbulent vertical momentum mixing, the latter referred to turbulent thermal wind balance.

A 3-D diagnostic framework called the TTW + ΩE system is developed for the secondary circulation and frontogenetic tendencies based on a momentum balance approximation that neglects ageostrophic tendencies. It is then applied to the idealized 2-D front and dense filament problems solved here.

In fronts the secondary circulation in the cross-front plane is a single overturning cell with downwelling on the dense side and upward buoyancy flux (implying density restratification and energy conversion from potential to kinetic). This is true for both strain-induced and TTW circulations. The horizontal buoyancy flux is mostly controlled by the direction of Ekman transport, and is therefore strongest for up- and down-front winds. The TTW circulation induces a frontogenetic tendency for velocity gradient near the surface on the dense side, while the tendency for surface buoyancy gradient is rather weak. The strain-induced circulation induces a strong surface frontogenetic tendency in both velocity and buoyancy on the dense side and in the centre of the front, respectively. For linear TTW circulations, the wind direction is inconsequential to the secondary-circulation strength except for extremely strong winds. However, with (nonlinear) ageostrophic advection, the TTW circulation is significantly stronger when the wind stress is in the SW direction relative to a northward geostrophic flow, and the frontogenetic tendency for velocity gradient is also much stronger. This wind direction causes a constructive reinforcement in the cross-front horizontal ageostrophic velocity between the Ekman and TTW circulations.

In dense filaments the secondary circulation is a pair of overturning cells with downwelling w in the centre for both strain-induced and TTW circulations. Again, the vertical buoyancy flux is upward, and the horizontal buoyancy flux is dominated by the Ekman transport. The frontogenetic tendency is positive for near-surface velocity at the filament centre and, with a strain-induced flow, also for buoyancy at the filament edges. Again, the linear TTW circulation is essentially independent of wind direction, but it is significantly strengthened by ageostrophic advection when the wind stress is in either the NE or SW directions.

In both of these flow configurations a positive frontogenetic tendency, especially for the velocity gradient near the surface, is a robust result in the SCFT analysis. This indicates that further evolution will contract the horizontal scale and increase the Rossby number and vertical velocity. Thus, a flow structure that begins as

submesoscale will evolve to be more deeply within the submesoscale range and thus become more prone to ageostrophic dynamics, including more rapidly growing frontal instabilities leading to further forward energy cascade to dissipation and diapycnal mixing.

Also in both submesoscale flow configurations, the vertical buoyancy flux is remarkably independent of wind direction and nonlinearity, while varying with the flow parameters as estimated in (4.19). It is an upward buoyancy flux whose primary effects are conversion of surface-layer available potential energy to submesoscale kinetic energy and an increase in density stratification within the surface layer (i.e. restratification flux). The horizontal buoyancy flux across the geostrophic flow by the secondary circulation is somewhat smaller than the vertical flux, but often larger when the Ekman transport is in that direction.

The secondary-circulation patterns are qualitatively similar between TTW solutions and strain-induced ones. For external strain, the cause of the secondary circulation is the confluent horizontal trajectories following the external deformation flow, and for TTW the cause is the cyclonically rotated obtuse angle direction for the surface ageostrophic flow in response to the vertical momentum mixing of the geostrophic shear in the surface boundary layer. This similarity of response between the two mechanisms continues into the nonlinear regime (not shown for α). It complicates the causal attribution in complex simulations or measurements, where generally both turbulent vertical mixing and mesoscale strain are present. On the other hand, there are noticeable differences in the $\mathcal{T}^b(x, z)$ patterns associated with TTW and strain (cf. figures 10 and 13*c*,*d*), although both causes induce positive frontogenesis near the surface. The scaling estimates in §§ 4 and 5, supported by the plotted $\mathcal{T}^b$ patterns, indicate that strain-induced frontogenesis is especially effective at sharpening submesoscale buoyancy gradients. Both frontogenetic mechanisms are effective at sharpening submesoscale velocity gradients in $\mathcal{T}^{\boldsymbol{u}}$.

When $Ro_g = \max[\zeta_g]/f_0$ approaches critical $O(1)$ values, the iterative solution procedure for the diagnostic secondary circulation fails to converge. This is suggestive, but not conclusive, of a breakdown of balanced dynamics and, because of the increasingly sharp horizontal gradient in w and ζ approaching the critical values, of an approach to spatial singularity. Beyond balanced dynamics lie inertia–gravity wave emissions, unbalanced frontal instabilities and turbulent forward energy cascade, all of which occur in realistic submesoscale simulations. Even there, however, the patterns of secondary circulation, buoyancy flux and frontogenetic tendency continue to resemble the patterns that arise in a SCFT balanced diagnostic analysis, indicating balanced dynamics continues to be relevant even where it is incomplete.

Beyond the present study much still needs to be learned about SCFT behaviours for upper-oceanic submesoscale fronts and filaments. The problems solved here have only a surface stress $\boldsymbol{\tau}$, and the inclusion of surface buoyancy flux $\mathcal{B}'$ will certainly alter the details of the boundary-layer turbulence. More fundamentally, this turbulent mixing can be resolved in large eddy simulations rather than parameterized, as here.

Acknowledgements

This research is supported by the Office of Naval Research (grant N000141410626) and the National Science Foundation (grant OCE-1355970).

Appendix A. Balanced potential vorticity and omega equations

These two equations are derived from the balanced model (2.11) before the velocity decomposition (2.14) is introduced.

The derivation path for the BVPE is defined by curl^z [horizontal momentum equations] $+ f_0\partial_z N^{-2}$ [buoyancy equation]. The result is

$$\begin{aligned}\mathrm{D}_g[Q_g] + \mathrm{curl}^z[\partial_z[\nu_v\partial_z \boldsymbol{u}]] \;=\; & \mathrm{curl}^z[\mathcal{N}^{\boldsymbol{u}}] + f_0\partial_z\left[\frac{\mathcal{N}^b}{N^2}\right] \\ & -\alpha(\partial_x v + \partial_y u) + f_0\partial_z\left[\frac{\partial_z[\kappa_v\partial_z b]'}{N^2}\right],\end{aligned} \tag{A 1}$$

where the quasigeostrophic potential vorticity is defined by

$$Q_g = \nabla^2\psi_g + f_0^2\partial_z\left[\frac{\partial_z\psi_g}{N^2}\right]. \tag{A 2}$$

The same convention of assigning left- and right-hand side terms is used here as in (2.11). The BPVE diagnoses the ψ_g tendency, hence also the b' tendency, when the 3-D elliptic operator in (A 2) is inverted.

The ΩE derivation path is $f_0\partial_z\,\mathrm{curl}^z$ [horizontal momentum equations] $-\nabla^2$ [buoyancy equation], and the result is

$$\begin{aligned}[f_0^2\partial_z^2 + N^2(z)\nabla^2]w \;=\; & -2f_0\boldsymbol{\nabla}\cdot J[\boldsymbol{\nabla}\psi_g, \partial_z\psi_g] \\ & + f_0\partial_z\,\mathrm{curl}^z[\partial_z[\nu_v\partial_z\boldsymbol{u}]] - \nabla^2[\partial_z[\kappa_v\partial_z b]'] \\ & + \mathcal{N}^{\Omega} + \alpha f_0\partial_z[\partial_x v + \partial_y u] + \alpha(\partial_{xx}b' - \partial_{yy}b'),\end{aligned} \tag{A 3}$$

where

$$\mathcal{N}^{\Omega} = -f_0\partial_z\,\mathrm{curl}^z[\mathcal{N}^{\boldsymbol{u}}] + \nabla^2\mathcal{N}^b. \tag{A 4}$$

The right-hand side terms with α and b' arise through the cancelation of the geostrophic vorticity and $\nabla^2 b'$ tendency terms as explained in appendix B. This ΩE is used as a replacement for the buoyancy equation in the SCFT system specified in § 2.1.

Appendix B. Derivations in deformation coordinates

As explained in § 2, the 3-D PE system (2.6) is written in deformation coordinates (X, Y, Z, T) and evaluated instantaneously with $\tilde{\beta} = 0$, which makes their derivatives formally equivalent to the derivatives in physical coordinates (x, y, z, t). However, further derived relations beyond (2.6) involving time derivatives must be done in the transformed coordinates before the instantaneous equivalence is declared. This is because ∂_T does not commute with $\partial_x = \mathrm{e}^{\tilde{\beta}}\partial_X$ and $\partial_y = \mathrm{e}^{-\tilde{\beta}}\partial_Y$, although all spatial derivatives are mutually commutative.

In the derivations of ΩE (2.20)–(2.21) and (A 3)–(A 4) from (2.11)–(2.13), it is necessary to cancel the geostrophic acceleration $\partial_T \boldsymbol{u}_g$ with the buoyancy tendency term to achieve a purely diagnostic relation. Starting from thermal wind balance expressed in transformed coordinates,

$$f\partial_Z v_g = \mathrm{e}^{\tilde{\beta}}\partial_X b, \quad f\partial_Z u_g = -\mathrm{e}^{-\tilde{\beta}}\partial_Y b, \tag{B 1a,b}$$

a time derivative is applied to obtain

$$f\partial_{ZT} v_g = \mathrm{e}^{\tilde{\beta}}\partial_{XT} b + \alpha\mathrm{e}^{\tilde{\beta}}\partial_X b, \quad f\partial_{ZT} u_g = -\mathrm{e}^{-\tilde{\beta}}\partial_{YT} b + \alpha\mathrm{e}^{-\tilde{\beta}}\partial_Y b. \tag{B 2a,b}$$

Then the operations are applied that lead toward ΩE, and the following result is obtained:

$$-f\mathrm{e}^{\tilde{\beta}}\partial_{ZXT}v_g + f\mathrm{e}^{-\tilde{\beta}}\partial_{ZYT}u_g = -[\mathrm{e}^{2\tilde{\beta}}\partial_{XXT}b + \mathrm{e}^{-2\tilde{\beta}}\partial_{YYT}b] - \alpha[\mathrm{e}^{2\tilde{\beta}}\partial_{XX}b - \mathrm{e}^{-2\tilde{\beta}}\partial_{YY}b]. \quad \text{(B 3)}$$

When this result is added to ∇^2 times the buoyancy equation, the terms proportional to $\partial_T b$ all cancel, as desired, and the second term in (B 3) is shifted over to the right-hand side, where it appears as the final term in $\mathcal{R}_O^{\Omega}$ in (2.21). All other terms in this ΩE derivation involve only spatial derivatives and thus are no different in form between the two coordinate systems.

To form the frontogenetic tendency equation for the buoyancy gradient (2.22), the following operation involving the buoyancy tendency is performed:

$$\begin{aligned}&\mathrm{e}^{\tilde{\beta}}\partial_X b\mathrm{e}^{\tilde{\beta}}\partial_X[\partial_T b] + \mathrm{e}^{-\tilde{\beta}}\partial_Y b\mathrm{e}^{-\tilde{\beta}}\partial_Y[\partial_T b]\\ &\quad = \partial_T\frac{1}{2}[(\mathrm{e}^{\tilde{\beta}}\partial_X b)^2 + (\mathrm{e}^{-\tilde{\beta}}\partial_Y b)^2] - \alpha[(\mathrm{e}^{\tilde{\beta}}\partial_X b)^2 - (\mathrm{e}^{-\tilde{\beta}}\partial_Y b)^2]. \end{aligned} \quad \text{(B 4)}$$

The final right-hand side term leads to the expression for $\mathcal{T}_\alpha^b$ in (2.22).

To form the frontogenetic tendency equation for the velocity gradient (2.23), the following operation involving the acceleration and the right-hand side deformation terms is performed on the horizontal momentum equations in (2.6):

$$\begin{aligned}&\mathrm{e}^{\tilde{\beta}}\partial_X u\mathrm{e}^{\tilde{\beta}}\partial_X[\partial_T u] + \mathrm{e}^{-\tilde{\beta}}\partial_Y u\mathrm{e}^{-\tilde{\beta}}\partial_Y[\partial_T u] + \mathrm{e}^{\tilde{\beta}}\partial_X v\mathrm{e}^{\tilde{\beta}}\partial_X[\partial_T v] + \mathrm{e}^{-\tilde{\beta}}\partial_Y v\mathrm{e}^{-\tilde{\beta}}\partial_Y[\partial_T v]\\ &\quad = \cdots + \alpha[(\mathrm{e}^{\tilde{\beta}}\partial_X u)^2 + (\mathrm{e}^{-\tilde{\beta}}\partial_Y u)^2 - (\mathrm{e}^{\tilde{\beta}}\partial_X v)^2 - (\mathrm{e}^{-\tilde{\beta}}\partial_Y v)^2]. \end{aligned} \quad \text{(B 5)}$$

The ... indicate all the other terms in these equations. Regrouping gives

$$\begin{aligned}&\partial_T\tfrac{1}{2}[(\mathrm{e}^{\tilde{\beta}}\partial_X u)^2 + (\mathrm{e}^{-\tilde{\beta}}\partial_Y u)^2 + (\mathrm{e}^{\tilde{\beta}}\partial_X v)^2 + (\mathrm{e}^{-\tilde{\beta}}\partial_Y v)^2]\\ &\quad - \alpha[(\mathrm{e}^{\tilde{\beta}}\partial_X u)^2 - (\mathrm{e}^{-\tilde{\beta}}\partial_Y u)^2 + (\mathrm{e}^{\tilde{\beta}}\partial_X v)^2 - (\mathrm{e}^{-\tilde{\beta}}\partial_Y v)^2]\\ &\quad = \cdots + \alpha[(\mathrm{e}^{\tilde{\beta}}\partial_X u)^2 + (\mathrm{e}^{-\tilde{\beta}}\partial_Y u)^2 - (\mathrm{e}^{\tilde{\beta}}\partial_X v)^2 - (\mathrm{e}^{-\tilde{\beta}}\partial_Y v)^2], \end{aligned} \quad \text{(B 6)}$$

or

$$\begin{aligned}&\partial_T\tfrac{1}{2}[(\mathrm{e}^{\tilde{\beta}}\partial_X u)^2 + (\mathrm{e}^{-\tilde{\beta}}\partial_Y u)^2 + (\mathrm{e}^{\tilde{\beta}}\partial_X v)^2 + (\mathrm{e}^{-\tilde{\beta}}\partial_Y v)^2]\\ &\quad = \cdots + 2\alpha[(\mathrm{e}^{\tilde{\beta}}\partial_X u)^2 - (\mathrm{e}^{-\tilde{\beta}}\partial_Y v)^2]. \end{aligned} \quad \text{(B 7)}$$

The right-hand side term here corresponds to $\mathcal{T}_\alpha^{\boldsymbol{u}}$ in (2.23).

Appendix C. The 2-D SCFT system

With the 2-D simplifications listed in § 3.1, the TTW and ΩE subsystems in (2.15)–(2.21) are

$$\left.\begin{gathered}-\partial_z[\nu_v\partial_z u_T] - f_0 v_T = \partial_z[\nu_v\partial_z u_O] - (u\partial_x + w\partial_z)u + \alpha u,\\ -\partial_z[\nu_v\partial_z v_T] + f_0 u_T = \partial_z[\nu_v\partial_z(v_g + v_O)] - (u\partial_x + w\partial_z)v - \alpha v,\\ \partial_x u_T + \partial_z w_T = 0,\\ w_T = 0 \quad \text{and} \quad \nu_v\partial_z\boldsymbol{u}_T = \frac{1}{\rho_0}\boldsymbol{\tau} - \nu_v\partial_z(\hat{\boldsymbol{y}}v_g + \boldsymbol{u}_O) \quad \text{at } z = 0,\\ \partial_z w_T = \boldsymbol{u}_T = 0 \quad \text{at } z = -H\end{gathered}\right\} \quad \text{(C 1)}$$

and

$$\left.\begin{aligned}[f_0^2\partial_z^2 + N^2(z)\partial_x^2]w_O = &-N^2(z)\partial_x^2 w_T + \alpha\partial_{xx}b' \\ &- \partial_x^2(u\partial_x + w\partial_z)b + \partial_x^2\partial_z[\kappa_v\partial_z b]', \\ \partial_x u_O + \partial_z w_O &= 0, \\ w_O &= 0 \quad \text{at } z = 0, \\ w_O &= -w_T \quad \text{at } z = -H, \\ w_O &\to 0 \quad \text{as } |x| \to \infty.\end{aligned}\right\} \tag{C 2}$$

The 2-D buoyancy- and velocity-gradient frontogenetic tendency equations (2.22) and (2.23), grouped in curly brackets by their identified contributing components, are

$$\begin{aligned}\mathrm{D}[\tfrac{1}{2}(\partial_x b')^2] \;=\; &\{0\} \\ &+ \{-N^2(\partial_x w)(\partial_x b') - (\partial_x b')((\partial_x u)(\partial_x b') + (\partial_x w)(\partial_z b'))\} \\ &+ \{\alpha(\partial_x b')^2\} \\ &+ \{(\partial_x b')\partial_x\partial_z(\kappa_v\partial_z b)\}\end{aligned} \tag{C 3}$$

and

$$\begin{aligned}\mathrm{D}[\tfrac{1}{2}((\partial_x u)^2 + (\partial_x v)^2)] \;=\; &\{-(\partial_x u)(\partial_x^2\phi')\} \\ &+ \{-(\partial_x u)(\partial_x \boldsymbol{u})\cdot(\partial_x \boldsymbol{u}) - (\partial_x w)(\partial_x \boldsymbol{u})\cdot(\partial_z \boldsymbol{u})\} \\ &+ \{2\alpha(\partial_x u)^2\} \\ &+ \{\partial_x \boldsymbol{u}\cdot\partial_x\partial_z[\nu_v\partial_z \boldsymbol{u}]\},\end{aligned} \tag{C 4}$$

with $\mathrm{D} = \partial_t + u\partial_x + w\partial_z$.

REFERENCES

BACHMAN, S. D. & TAYLOR, J. R. 2016 Numerical simulations of the equilibrium between eddy-induced restratification and vertical mixing. *J. Phys. Oceanogr.* **46**, 919–935.

BERGERON, T. 1928 Über die dreidimensional verknüpfende Wetteranalyse I. *Geophys. Publ.* **5**, 1–111.

CRAIK, A. D. D. & LEIBOVICH, S. 1976 A rational model for Langmuir circulations. *J. Fluid Mech.* **73**, 401–426.

CRONIN, M. F. & KESSLER, W. S. 2009 Near-surface shear flow in the Tropical Pacific cold tongue front. *J. Phys. Oceanogr.* **39**, 1200–1215.

ELIASSEN, A. 1962 On the vertical circulation in frontal zones. *Geophys. Publ.* **24**, 147–160.

FLIERL, G. & MIED, R. 1985 Frictionally induced circulations and spin down of a warm-core ring. *J. Geophys. Res. Oceans* **90**, 8917–8927.

FOX-KEMPER, B., FERRARI, R. & HALLBERG, R. W. 2008 Parameterization of mixed layer eddies. Part I: theory and diagnosis. *J. Phys. Oceanogr.* **38**, 1145–1165.

GARRETT, C. J. R. & LODER, J. W. 1981 Dynamical aspects of shallow sea fronts. *Phil. Trans. R. Soc. Lond.* **302**, 563–581.

GULA, J., MOLEMAKER, M. J. & MCWILLIAMS, J. C. 2014 Submesoscale cold filaments in the Gulf Stream. *J. Phys. Oceanogr.* **44**, 2617–2643.

HOSKINS, B. J. 1982 The mathematical theory of frontogenesis. *Annu. Rev. Fluid Mech.* **14**, 131–151.

HOSKINS, B. J. & BRETHERTON, F. P. 1972 Atmospheric frontogenesis models: mathematical formulation and solution. *J. Atmos. Sci.* **29**, 11–37.

LARGE, W. G., MCWILLIAMS, J. C. & DONEY, S. C. 1994 Oceanic vertical mixing: a review and a model with a nonlocal boundary layer parameterization. *Rev. Geophys.* **32**, 363–403.

MAHADEVAN, A. & TANDON, A. 2006 An analysis of mechanisms for submesoscale vertical motion at ocean fronts. *Ocean Model.* **14**, 241–256.

MCWILLIAMS, J. C. 2003 Diagnostic force balance and its limits. In *Nonlinear Processes in Geophysical Fluid Dynamics* (ed. O. U. Velasco Fuentes, J. Sheinbaum & J. Ochoa), pp. 287–304. Kluwer Academic Publishers.

MCWILLIAMS, J. C. 2016 Submesoscale currents in the ocean. *Proc. R. Soc. Lond.* A **472**, 20160117,1–32.

MCWILLIAMS, J. C., COLAS, F. & MOLEMAKER, M. J. 2009 Cold filamentary intensification and oceanic surface convergence lines. *Geophys. Res. Lett.* **36**, L18602.

MCWILLIAMS, J. C., GULA, J., MOLEMAKER, M. J., RENAULT, L. & SHCHEPETKIN, A. F. 2015 Filament frontogenesis by boundary layer turbulence. *J. Phys. Oceanogr.* **45**, 1988–2005.

MCWILLIAMS, J. C., HUCKLE, E. & SHCHEPETKIN, A. F. 2009*a* Buoyancy effects in a stratified Ekman layer. *J. Phys. Oceanogr.* **39**, 2581–2599.

MCWILLIAMS, J. C., MOLEMAKER, M. J. & OLAFSDOTTIR, E. I. 2009*b* Linear fluctuation growth during frontogenesis. *J. Phys. Oceanogr.* **39**, 3111–3129.

MCWILLIAMS, J. C., RESTREPO, J. M. & LANE, E. M. 2004 An asymptotic theory for the interaction of waves and currents in coastal waters. *J. Fluid Mech.* **511**, 135–178.

MCWILLIAMS, J. C., YAVNEH, I., CULLEN, M. J. P. & GENT, P. R. 1998 The breakdown of large-scale flows in rotating, stratified fluids. *Phys. Fluids* **10**, 3178–3184.

NAGAI, T., TANDON, A. & RUDNICK, D. L. 2006 Two-dimensional ageostrophic secondary circulation at ocean fronts due to vertical mixing and large-scale deformation. *J. Geophys. Res.* **111**, C09038.

NIILER, P. P. 1969 On the Ekman divergence in an oceanic jet. *J. Geophys. Res.* **74**, 7048–7052.

PONTE, A. L., KLEIN, P., CAPET, X., LE TRAON, P.-Y., CHAPRON, B. & LHERMINIER, P. 2013 Dagnosing surface mixed layer dynamics from high-resolution satellite observations: numerical insights. *J. Phys. Oceanogr.* **43**, 1345–1355.

STERN, M. E. 1965 Interaction of a uniform wind stress with a geostrophic vortex. *Deep-Sea Res.* **12**, 355–367.

SULLIVAN, P. P. & MCWILLIAMS, J. C. 2016 Frontogenesis and frontal arrest for a dense filament in the surface boundary layer. *J. Fluid Mech.*; (submitted).

SUZUKI, N., FOX-KEMPER, B., HAMLINGTON, P. E. & VAN ROEKEL, L. P. 2016 Surface waves affect frontogenesis. *J. Geophys. Res. - Oceans* **121**, 1–28.

TAYLOR, J. R. & FERRARI, R. 2009 On the equilibration of a symmetrically unstable front via a secondary shear instability. *J. Fluid Mech.* **622**, 103–113.

THOMAS, L. N. 2005 Destruction of potential vorticity by winds. *J. Phys. Oceanogr.* **35**, 2457–2466.

THOMPSON, L. 2000 Ekman laers and two-dimensional frontogenesis in the upper ocean. *J. Geophys. Res.* **105**, 6437–6451.

WENEGRAT, J. O. & MCPHADDEN, M. J. 2016*a* A simple analytical model of the diurnal Ekman layer. *J. Phys. Oceanogr.* **46**, 2877–2894.

WENEGRAT, J. O. & MCPHADDEN, M. J. 2016*b* Wind, waves, and fronts: frictional effects in a generalized Ekman model. *J. Phys. Oceanogr.* **46**, 711–747.